Masterarbeit

Structure of Water on Nitrogen-doped Graphene from First-principles Molecular Dynamics

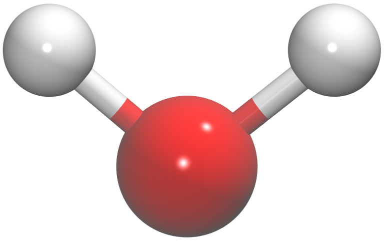

Svenja Johanna Wörner

Eingereicht am 03.07.2015

Durchgeführt am Max-Planck-Institut für Polymerforschung und dem
Physikalisch-Chemischen Institut der Ruprecht-Karls-Universität
Heidelberg unter der Leitung von Prof. Dr. D. Donadio,
Prof. Dr. K. Kremer und Prof. Dr. A. Dreuw

Contents

1. Introduction

Novel nitrogen-doped graphene catalysts have been examined toward their ability to split water into hydrogen and oxygen. The catalytic activity was confirmed experimentally and two catalytic active doping patterns were identified. Three doped and one undoped graphene surface were simulated using molecular dynamics (MD) to gain more insight into the catalytic activity of the surfaces. The results show, that the interaction between the water and the graphene sheet with the pyridine-type nitrogen pattern is much more pronounced than for the substitutional nitrogen-doping pattern. This indicated, that the catalytic activity of the nitrogen-doped graphene materials originates from pyridine-type structures in the graphene sheets, rather than from substitutional nitrogen atoms.

1.1. Background

Hydrogen is the simplest and most abundant element in the universe. It simply consists of one proton and one electron. On Earth one in six atoms is a hydrogen atom but only traces of molecular hydrogen can be found. Most of the hydrogen is bound in water or organic molecules, making them the main sources for hydrogen production on industrial level.[1]

The annual worldwide hydrogen production amounts to $6 \cdot 10^{11} m^3$.[2] Almost the entire production is used by the chemical industry itself again. There are two main industrial production techniques for hydrogen. It can either be obtained from organic molecules via thermochemical processes or through electrolysis of water. Hydrogen is also a byproduct of the chloralkali process for the production of chlorine and sodium hydroxide. Half of the annual hydrogen is produced through steam reforming. Other thermochemical processes are natural gas and renewable liquid fuel reforming and coal and biomass gasification. All these thermochemical processes have one problem in common, they also generate the green house gas carbon dioxide.

The first step in the steam reforming process is the so called steam reforming reaction of methane from natural gas or mineral oil (equation 1.1):

$$CH_4 + H_2O \longrightarrow CO + 3H_2 \tag{1.1}$$

It is similar for all thermochemical processes, since not only methane but also other hydrocarbons and coal can react with water to form carbon monoxide and hydrogen.

In a subsequent step the carbon monoxide produced is further oxidized to carbon dioxide in the so called water-gas shift reaction (equation 1.2):

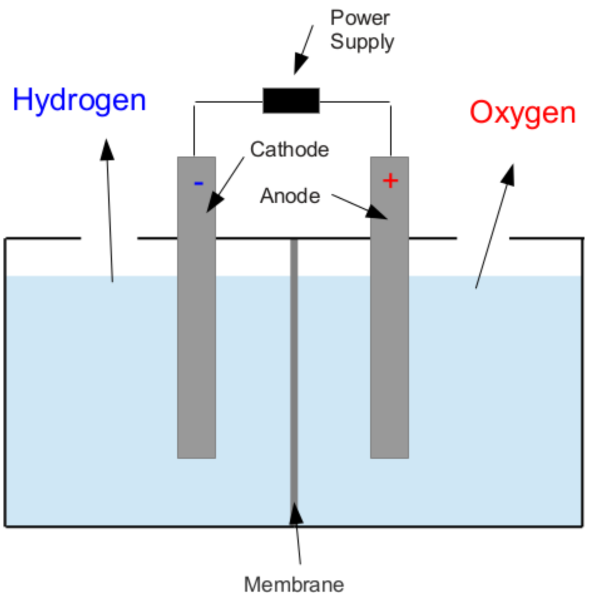

Figure 1.1.: Conceptual scheme of electrolysis cell.

$$CO + H_2O \rightleftharpoons CO_2 + H_2 \tag{1.2}$$

The second step is the same for all thermochemical processes and it is carried out to remove the highly toxic carbon monoxide. Both reactions require expensive transition metal catalysts sensitive to sulfur poisoning.

The electrolysis process on the other hand uses electricity to split water into hydrogen and oxygen (equation 1.3).

$$2H_2O \longrightarrow 2H_2 + O_2 \tag{1.3}$$

This process does not produce any carbon dioxide directly, which makes it an environmentally friendly hydrogen production process. The electrolysis process is carried out in an electrolyzer. The conceptual scheme of an electrolyzer is shown in figure 1.1. It consists of two electrodes connected to a power supply. The electrolyte (blue) is a liquid in which the ions move towards the electrodes. The oxidation reaction of oxygen in water occurs at the anode, which is positively charged (equation 1.4). The reaction yields oxygen and hydroxyl cations which move towards the cathode through the membrane. The electrons move through the external circuit enforced by the power supply to the cathode. The reduction reaction then occurs at the cathode (equation 1.5), yielding hydrogen and water. Different electolyzers differ by the materials used for the electrodes, membranes and electrolytes.

$$6H_2O \longrightarrow O_2 + 4H_3O^+ + 4e^- \tag{1.4}$$

$$4H_3O^+ + 4e^- \longrightarrow 2H_2 + 4H_2O \tag{1.5}$$

Equations 1.4 and 1.5 describe the four electron-transfer pathway for water splitting.[3] The redox-potential between the two reactions equals 1.23 V. [4] The reaction in equation 1.5 is defined as 0 V as it is the reaction occurring at the normal hydrogen electrode (NHE). The redox-potential equals the so called decomposition potential, the voltage needed to decompose the molecule theoretically. Due to kinetic restraints additional energy is needed to enforce the reaction. This additional voltage is called overpotential. The overpotential depends on the electrode material used for the specific reaction.

The electrolysis process, however, has two interdependent problems that limit its efficiency and therefore its large scale application. First of all, the overpotential for the oxygen evolution reaction (OER) (equation 1.4) at the anode is typically very high (> 450 mV).[5] Therefore the choice of materials for the anodes is critical. Commercial electrolyzers use nickel anodes in hot alkaline solutions.[5] Low overpotentials and high catalytic activity can be achieved with so called dimensionally stable anodes (DSA), which consist of ruthenium and/or iridium oxide on an inert support such as titanium.[6] Similar and also highly reactive and stable catalysts also contain rhodium and iridium oxide stabilized by inert metal oxides of less expensive metals, such as TiO_2, SnO_2, Ta_2O_5, or ZrO_2.[7] Rhodium and iridium are very rare and expensive metals though, making the electrolysis process more expensive compared to the hydrogen production from fossil fuels. This is the second problem, tightly connected to the solution of the first problem of the high overpotential. Catalysts with more earth-abundant metals usually feature manganese and cobalt.[3, 8–14] Catalysts based on hydroxides or oxides of those two materials have a lower catalytic efficiency than rhodium and iridium based catalysts. Non-metallic systems, such as nitrogen-doped carbon materials, show the ability to catalyze the OER with an overpotential comparable to the metal-based catalysts (380 mV overpotential).[15] Since they do not contain any precious metals their production is inexpensive, while exhibiting the same properties in the OER as metal-based catalysts.

Utilizing hydrogen as an energy carrier seems very promising and both the US and the European Union are aiming to promote the use of hydrogen as an alternative energy carrier to fossil fuels.[16, 17] Electrolysis from water is a favored production technology, since it does not produce any green house gases itself. Depending on the source of electricity used, this technology does not produce green house gases at all. One of the possible applications is storing excess electricity produced from renewable energy sources such as wind or solar energy by producing hydrogen via electrolysis. This hydrogen could be used for production of electricity again or used in fuel cells for heating and transportation. For all these applications, the efficiency of the electrolysis process for hydrogen production needs to be improved and inexpensive and yet efficient electrode materials, such as doped graphitic carbon, need to be understood and further developed.

1.2. Water Splitting Experiments on Nitrogen-Doped Graphene

Nitrogen-doped graphene is a promising material for hydrogen production: it is stable, versatile and relatively inexpensive. After the success as a catalyst for the oxygen reduction reaction (ORR, equation 1.6),

$$O_2 + 4H^+ + 4e^- \longrightarrow 2H_2O \tag{1.6}$$

nitrogen-doped graphene was employed as a catalyst for the oxidation of water, the so called oxygen evolution reaction (OER, equation 1.7), or simply the water-splitting reaction.[15, 18–21]

$$2H_2O \longrightarrow O_2 + 4H^+ + 4e^- \tag{1.7}$$

An effective approach to synthesize nitrogen-doped carbon (N/C) materials was developed by Zhao *et al.* and consists of three steps.[15] The process is schematically shown in figure 1.2.

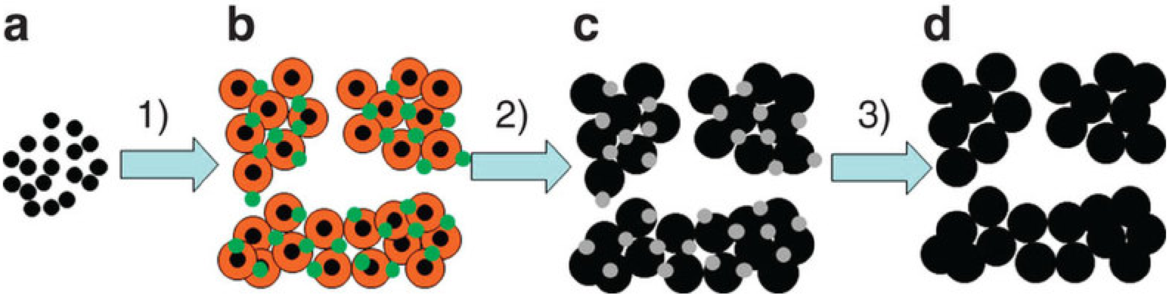

Figure 1.2.: Synthesis of the nitrogen-doped graphene catalyst. (Reprinted by permission from Macmillan Publishers Ltd: Zhao *et al.*, *Nature Communications* **4**, 2390, copyright 2013.)

First, a melamine formaldehyde polymer **b** is synthesized from nickel nitrate and carbon particles **a**. Then the carbon particles, covered with the melamine formaldehyde polymer and nickel nitrate, are pyrolyzed at different temperatures in a range of 700 to 1000°C. The pyrolysis temperature can be used to regulate the nitrogen concentrations. The higher the temperature, the lower the nitrogen concentration in the sample. This produces nitrogen-doped graphene with nickel-oxide particles **c**. In a last step the pyrolyzed samples are leached with hydrochloride acid to remove the nickel oxide and obtain the nitrogen-doped graphene catalyst **d**.

Physical characterization showed, that the nitrogen-doped graphene samples were free of nickel and the catalytic activity is therefore attributed to the nitrogen sites in the graphene structure. Figure 1.3a shows the oxygen evolution activity of different electrode materials. The commercial platinum electrode used shows the lowest catalytic activity. As mentioned previously, the overpotential for these electrodes is very high, limiting their efficiency. The unleached nitrogen-doped sample still contains

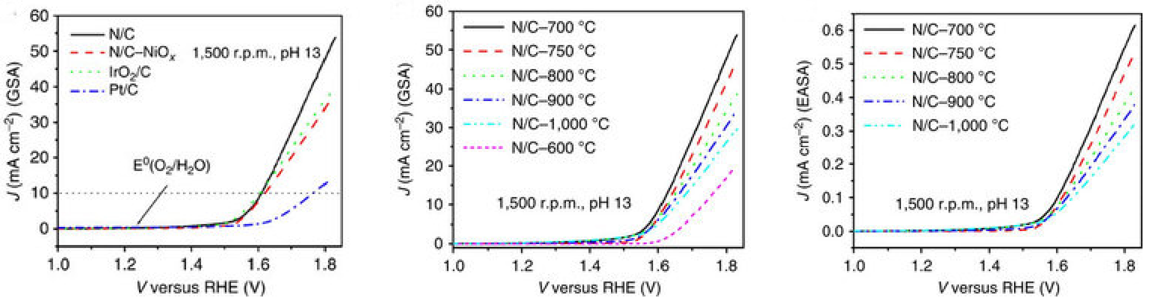

(a) **(b)** **(c)**

Figure 1.3.: The current density of the OER of (a) the leached and unleached N/C materials compared to other common electrode materials and (b)+(c) show the comparison of the N/C catalysts pyrolyzed at different temperatures evaluated with two different methods ((b)-GSA, (c)-EASA).(Reprinted by permission from Macmillan Publishers Ltd: Zhao *et al.*, *Nature Communications* **4**, 2390, copyright 2013.)

nickel oxide species and has a catalytic reactivity comparable to electrodes containing iridium oxide.[22] They have a much lower overpotential than the platinum electrode, since their catalytic activity sets in at a lower potential. The leached and therefore nickel-free nitrogen-doped carbon electrode has the highest catalytic activity and an overpotential comparable to the unleached sample and the iridium oxide containing electrode. The catalytic activity can thus not originate from nickel sites in the graphene sheets and the nitrogen sites are responsible for the catalytic activity. This was verified by repeating the experiment with a pure graphene electrode, which did not show any catalytic reactivity in the OER.

The catalytic activities of the nitrogen-doped and leached samples pyrolyzed at different temperatures are shown in figure 1.3b and 1.3c using two different methods. The sample pyrolyzed at 700°C showed the highest catalytic activity in the OER with the lowest overpotential. Increasing the pyrolysis temperature decreases the nitrogen content and also the catalytic activity. A lower pyrolysis temperature of 600°C showed a lower catalytic activity and a high overpotential due to high electrical resistance.

A nitrogen content of 4.1% was measured by X-ray photoelectron spectroscopy (XPS) for the most reactive sample pyrolyzed at 700°C. Three different structures for the nitrogen doping in the samples were identified in the XPS spectra. A pyridinic and substitutional nitrogen structure and a less common pyridinic-N$^+$O$^-$ structure. Since the catalytic activity increased with an increasing number pyridinic and substitutional nitrogen defect structures, the catalytic activity was attributed to those two nitrogen active centers. The different types of possible nitrogen doping patterns in graphene will be discussed in the next section 1.3.

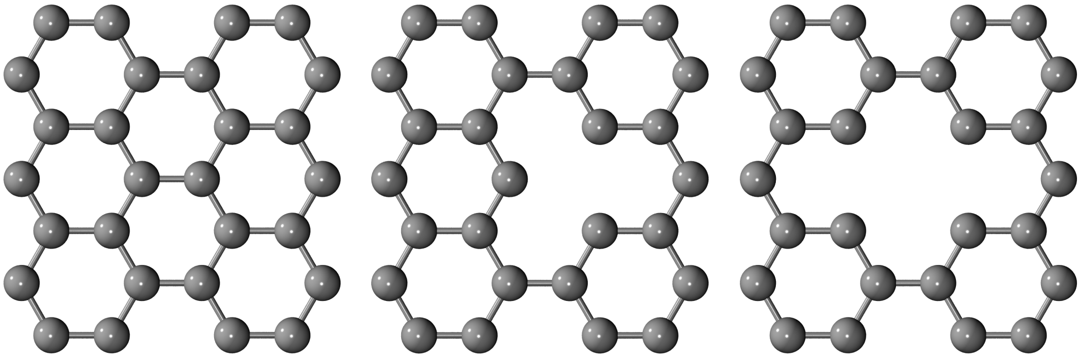

(a) pure graphene sheet (*pure*) **(b)** monovacancy (*mono*) **(c)** divacancy (*div*)

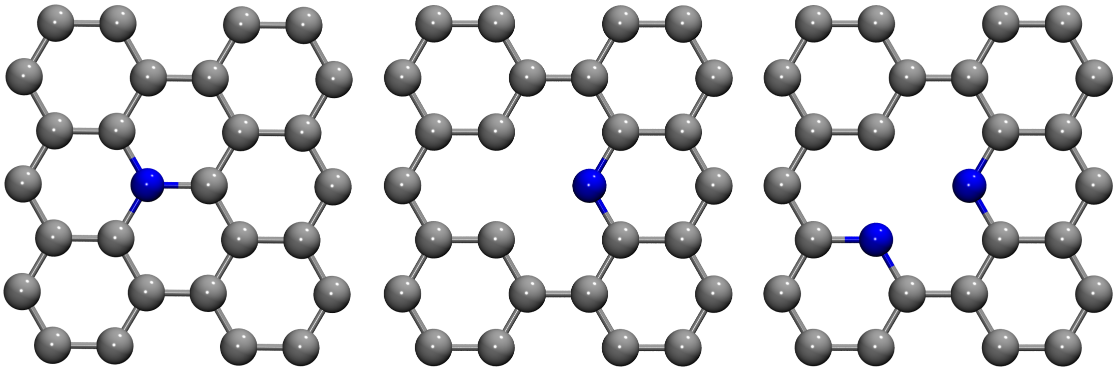

(d) substitutional nitrogen defect (*subst*) **(e)** monomeric pyridine-type defect (*monoPy*) **(f)** dimerized pyridine-type defect (*diPy*)

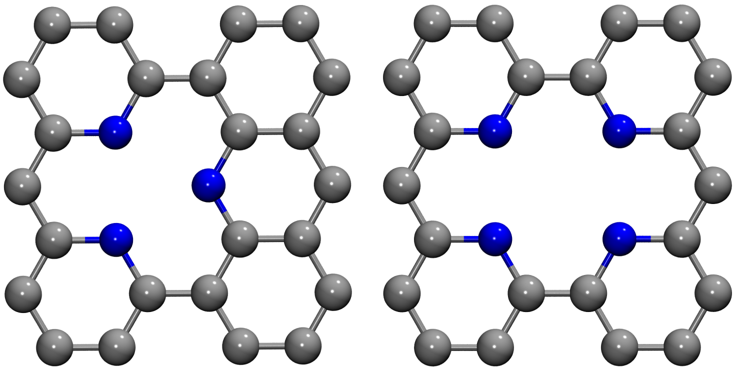

(g) trimerized pyridine-type defect (*triPy*) **(h)** tetramerized pyridine-type defect (*tetraPy*)

Figure 1.4.: Defect structures of pure and nitrogen-doped graphene as studied by Fujimoto *et al.*.[23] Respective abbreviations are included in parentheses.

1.3. Nitrogen-doping in Graphene

Doping materials is a very common way to influence their electronic and chemical properties. Fujimoto *et al.* studied nitrogen doping patterns in comparison to nitrogen-free defect structures in graphene theoretically.[23] They determined not only the overall stability but also relative stability of the different doping patterns.

There are two possible defect structures in a perfect graphene sheet as shown in figure 1.4a. Either one carbon atom can be missing from the perfect honeycomb structure yielding a monovacancy as shown in figure 1.4b. Or two adjacent carbon atoms can be missing from the structure forming a divacancy (figure 1.4c). Doping a graphene surface can lead to 5 possible structures. A carbon atom from the honeycomb structure can simply be replaced by a nitrogen atom. This structure is called a substitutional nitrogen defect or quaternary- or graphitic-N, as shown in figure 1.4d (abbreviation "subst"). The other possibility is a pyridine-type structure around a mono- or divacancy. Depending on the number of carbon atoms replaced around the vacancy the structures are called monomeric, dimerized, trimerized or tetramerized pyridine-type defect and the structures are shown in figures 1.4e, 1.4f, 1.4g, and 1.4h, respectively. They are abbreviated as monoPy, diPy, triPy and tetraPy, respectively.

The formation energy of these nitrogen-induced defect structures is defined in equation 1.8.

$$E_f = E_{tot} - m_C \mu_C - m_N \mu_N \tag{1.8}$$

E_{tot} is the total energy of the doped graphene surface in the supercell and m_C and m_N are the number of carbon and nitrogen atoms in the supercell. μ_C and μ_N are the chemical potentials of carbon and nitrogen. Graphene is used as a reference system for carbon and the N_2 molecule as reference system for nitrogen. The chemical potential is the energy per atom of the reference system. The formation energies for the five nitrogen-doped structures are listed in table 1.1.

Table 1.1.: Formation energies of different defect structures in nitrogen-doped graphene surfaces (in [eV]).[23] Columns from left to right: substituional nitrogen defect, monomeric, dimerized, trimerized, and tetramerized pyridine-type defect.

subst	monoPy	diPy	triPy	tetraPy
0.32	5.61	4.28	2.51	2.55

The formation energy for the substitutional nitrogen defect ((d)) is significantly lower than for all the pyridine-type structures. It is therefore the most stable of all the nitrogen defects. Among the pyridine-type defects the trimerized structure around the monovacancy and tetramerized structure around the divacancy are the most stable structures ((g) and (h), respectively). The structures for the monomeric and dimerized pyridine-type defects feature two and one carbon atom not embedded in the honeycomb structure but pointing toward the vacancy. These structures are less stable than the trimerized and tetramerized pyridine-type defects, where all corner atoms pointing toward the vacancy are substituted by a nitrogen atom.

Table 1.2.: Relative Energies of nitrogen-defect structures in graphene [eV].[23]

E_1 (eq. 1.9)	E_2 (eq. 1.10)	E_3 (eq. 1.11)	E_4 (eq. 1.12)
-6.76	-7.13	-3.75	-2.10

Fujimoto *et al.* also calculated relative energies to determine which defect structure was most likely to be formed from defects already being present in the graphene sheet. The definitions of the relative energies are given in equations 1.9 to 1.12 and the results are reported in table 1.2.

$$E_1 = E_{triPy} + E_{pure} * 3 - [E_{subst} * 3 + E_{mono}] \tag{1.9}$$

The relative energy E_1 shows the difference between the trimerized pyridine-type type defect and the substitutional pattern, where E_{pure} is the energy of the pure, undoped graphene surface and E_{mono} the energy of a graphene surface with a monovacancy. The trimerized pyridine-type structure is more favorable by 6.76 eV than the substitutional pattern, if a monovacancy is present in the graphene sheet.

$$E_2 = E_{triPy} + E_{pure} * 3 - [E_{subst} * 3 + E_{div} + \mu_C] \tag{1.10}$$

The relative energy E_2 compares the trimerized pyridine-type defect with the substitutional pattern in presence of a divacancy, where E_{div} is the energy of undoped graphene with a divacancy and μ_C is the energy per atom in a pristine graphene surface. The trimerized-pyridine type defect is also more stable in presence of a divacancy, by 7.13 eV.

$$E_3 = E_{triPy} + E_{pure} * 2 - [E_{subst} * 2 + E_{monoPy}] \tag{1.11}$$

$$E_4 = E_{triPy} + E_{pure} - [E_{subst} + E_{diPy}] \tag{1.12}$$

The relative energies E_3 and E_4 compare the stabilities of the monomeric and dimerized pyridine-type defects, respectively, with the trimerized pyridine-type defect. Both are more likely to form a trimerized pyridine-type structure, if two or one additional substitutional nitrogen atom are present. The trimerized pyridine-type structure is more stable by 3.75 eV than a monomeric pyridine-type defect in the presence of two substituional nitrogen defects. And it is more stable by 2.10 eV than a dimerized pyridine-type structure in the presence of a substituional nitrogen atom in the graphene surface.

These results suggest, that despite the substituitional nitrogen pattern being the most stable structure, trimerized pyridine-type structures are more likely to form, once a vacancy is present. The trimerized pyridine-type structure is also more stable than monomeric or dimerized structures upon presence of substituional nitrogen atoms. The small difference in the formation energies of trimerized and tetramerized pyridine-type structures suggest, that both are more likely doping structures, than the substitutional nitrogen-doping patter in graphene.

1.4. Confined Water

The interaction of water with various surfaces has been a field of intensive study.[19, 21, 24–27] Therefore only a short overview can be given.

Cicero at al. studied water confined between two graphene sheets or inside carbon nanotubes.[26] They studied structural as well as dynamical properties of the systems. Since carbon nanotubes are not studied in this project, the results for these systems will not be mentioned.

The systems contain a water bulk confined between two graphene sheets at different graphene-graphene distances. Three confinement distances were studied: 10.09 Å, 14.41 Å and 25.02 Å. Between the graphene sheets at the aforementioned distances 32, 54 and 108 water molecules are confined, respectively. To choose the proper interlayer separation, the distance between the graphene sheets was altered, while the number of water molecules was not changed. The interlayer distance was altered until the pressure of the water had reached atmospheric pressure. For computational reasons explained in chapter 2, deuterium was used instead of hydrogen.

Since the interest of the simulations were on the different confinement distances and the simulation of the doped graphene surfaces here were carried out at a fixed distance of 14.41 Å, only this confinement distance will be discussed in detail. The results for the other confinement distances are similar. The confinement has little effect on the structure of the water and the effects are due to the interaction between the water and the interface.

Figure 1.5 shows the mass density profile in the top panel, the electronic density in the middle and the number of hydrogen bonds in the bottom panel. All densities are in z-direction perpendicular to the graphene surface and for the system with an interlayer separation of 14.41 Å. The mass density profile shows the density of the oxygen and deuterium atoms separately. The profile shows an exclusion volume of about 2.5 Å from the graphene surface, where no water is present. Then two surface layers with a density higher than the bulk value can be observed. These surface layers are about 5 Å thick. In between the two surface layers the density oscillates around the bulk value of 1 g/cm^3. This behavior is normal for water confined between hydrophobic and hydrophylic surfaces.[28–30] The mass densities of oxygen and deuterium display one distinct difference. The deuterium profile exhibits a small shoulder in the exclusion volume. This gives information about the orientation of water molecules in the surface layers. Some water molecules point toward the surface with one O-D bond.

The electron density displays a similar structure. The water electron density shows the two surface layers with a slightly increased density compared to the bulk layer. The declining electron density within the exclusion volume is attributed to the weak interaction with the graphene surface.

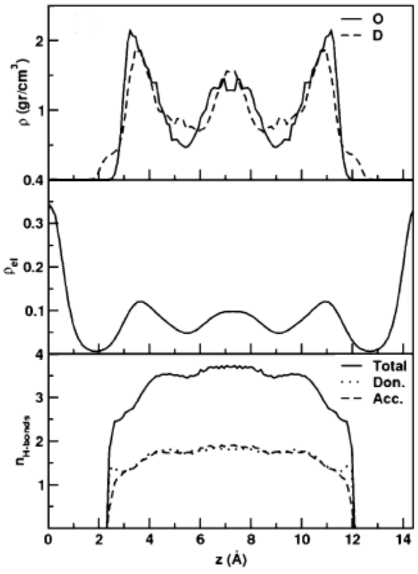

Figure 1.5.: The mass density profile (top), electron density profile (middle), and average number of hydrogen bonds (bottom) of 54 water molecules confined between two graphene sheets at a distance of 14.41 Å. (Reprinted with permission from Cicero *et al.*, *Journal of the American Chemical Society* **130**, 1871. Copyright 2008 American Chemical Society.)

The bottom panel shows the average number of hydrogen bonds and the average number of donor and acceptor water molecules. The interfacial layers have a slightly smaller number of hydrogen bonds in average. The average number of hydrogen bonds is up to 70% of the bulk value even though they are only surrounded by half the number of water molecules as in the bulk. The curve for the donor water molecules also displays a small shoulder, indicating that water molecules in the interfacial layer are more likely to be hydrogen-bond acceptors, since one O-D bond is dangling toward the surface.

This structural information is supported by the study of IR spectra of confined water by Sharma *et al.*(figure 1.6).[25] As the confinement distance decreases, the fraction of water molecules in the interfacial layer with one O-D bond pointing toward the surface increases. The number of molecules in the surface layers increase with respect to the number of atoms in the bulk layer with decreasing confinement distance. Since the dangling O-D bonds do not engage in hydrogen bonding, the O-D stretching frequency decreases with increasing confinement length. This is indicated by the arrows in the high-frequency region of the spectrum in figure 1.6. The arrows in the low-frequency region show the red shift for the modes from hindered translations with decreasing confinement distance (figure 1.6). The inset of figure 1.6 shows the comparison between the IR spectrum of the confinement length of 25.02 Å with that of bulk water (thick line). The shoulder emphasized by the arrow arises from the broken hydrogen bonds in the interfacial layer as well.

All in all, these results show, that the confinement has little effect on the structure

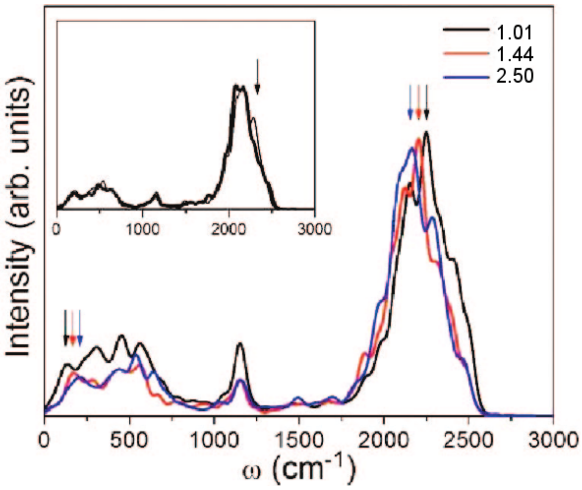

Figure 1.6.: The IR spectrum of water confined at 1.01 nm (black line), 1.44 nm (red line), and 2.5 nm (blue line). The inset shows the comparison of the IR spectrum of bulk water (thick line) with that of the system with the confinement distance of 2.5 nm (thin line).(Reprinted with permission from Sharma *et al.*, *Nano Letters* **8**, 2959. Copyright 2008 American Chemical Society.)

of liquid water beyond the first water layer interacting with graphene. The structural differences between the interfacial layers and the bulk water arise solely from the interaction of the water with the surface itself.

1.5. Motivation

The novel graphene materials introduced by Zhao *et al.* are inexpensive and yet efficient catalysts for the OER (equation 1.7).[15] They clearly identified nitrogen doping as the source for catalytic activity by comparing the catalytic activity with that of an undoped surface and that of an unleached graphene sheet still containing nickel oxide from the precursor material. Nitrogen doping in the graphene materials occurs in three patterns, in a substitutional pattern and a pyridine-type pattern around a vacancy. And additionally, a substitutional-N^+-O^- species can be found in the samples. The catalytic activity is attributed to these first two doping patterns. The interaction of water with these active cententers is of great interest for understanding the water splitting process on these doped graphene materials. Insight into the splitting process can be used to develop more efficient materials for the production of oxygen from water, since this is the step of the electrolysis that limits its efficiency in the hydrogen production.

The works of Fujimoto *et al.* show the different stabilities among the nitrogen-doping patterns. And taking this into account the most stable doping pattern were examined with respect to the water splitting activity. The most stable nitrogen-doping patterns in graphene are the substitutional pattern (figure 1.4d) and the trimerized and tetramerized pyridine-type patterns (figures 1.4g and 1.4h, respectively). These are not only the most stable and likely patterns, but also the nitrogen-doping structures which are held responsible for the catalytic activity of the nitrogen-doped graphene materials.

The computational setup of Cicero *et al.* for the confined water is very reasonable. The behavior of confined water is well characterized between undoped graphene sheets and is reasonable for a comparison with the experimental setup. The structural and dynamic characterization by Cicero *et al.*, as well as the study of infrared spectra of these systems by Sharma *et al.*, show that the effect of confinement is very localized in the interfacial layers.[25, 26] Smaller confinement distances show some size effects, but a confinement distance of 14.41 Å is not biased by confinement and size effects. A setup with a confinement distance of 14.41 Å is therefore suitable for studying the interaction between water and nitrogen-doped graphene surfaces.

In this thesis *ab initio* molecular dynamics (MD) simulations are used to study the structure and dynamics of water at the interface with nitrogen-doped graphene. We use a setup similar to the one described above, in which water is confined between graphene planes at 1.4 nm distance, and we consider systems with different types of nitrogen-defects, with concentration between 3.3 and 6.7%. These results are compared to the case of water confined between pure graphene surfaces, and they provide key elements to interpret the enhanced efficiency of N-doped graphene as a catalyst of the Hydrogen production related reactions in terms of the interactions between N-defects and water.

The following chapter 2 describes the computational methods and analysis procedures used. As well as the specific programs and settings used for the calculations. Chapter 3 describes and discusses the results of the Molecular Dynamics simulations of the confined water systems. A summary of the work and perspectives on further work are given in the last chapter 4.

2. Computational Methods

This chapter describes the computational techniques and analysis methods used, as well as the parameters used for the simulations.

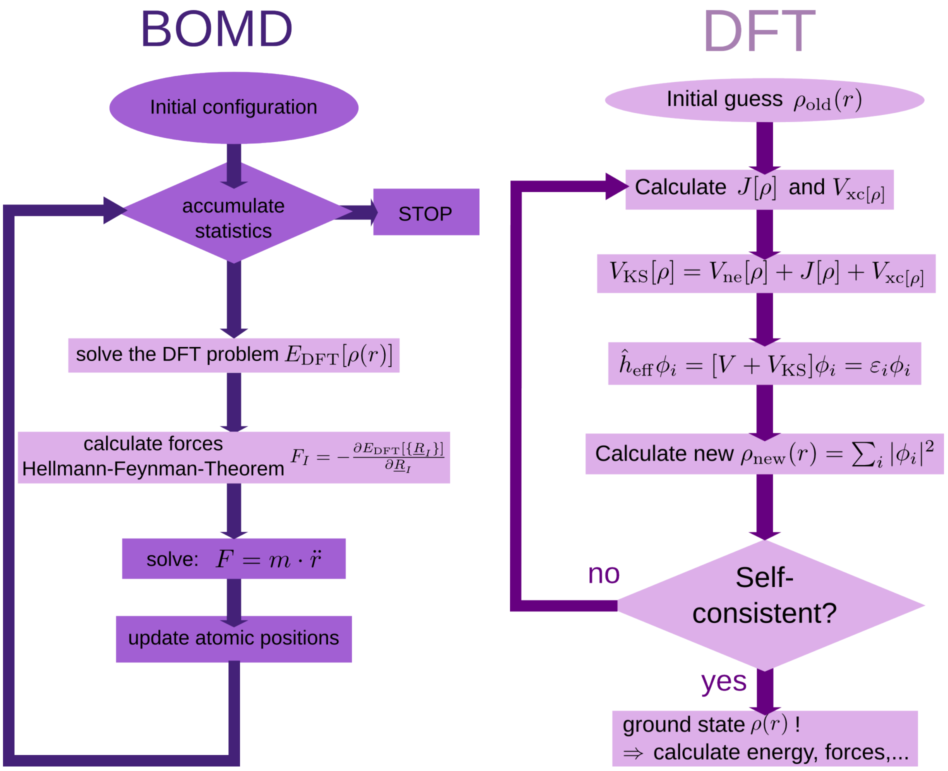

(a) **(b)**

Figure 2.1.: Schematic flowchart representing (a) the steps of a Born-Oppenheimer molecular dynamics simulations and (b) the steps of a density functional theory calculation employed within the BOMD scheme.

2.1. Density Functional Theory

Density functional theory (DFT) is used to compute the ground state electronic density n(r) and the ground state energy E_{DFT}. The general approach is given in figure 2.1b. The energy is used for the *ab intio* molecular dynamics (AIMD) simulations described in section 2.2.

One of the most fundamental approximations made by DFT is the Born-Oppenheimer approximation. The Born-Oppenheimer approximation states, that due to the large difference in mass of electrons and nuclei, the nuclei move much slower than the electrons. Therefore the wavefunction and the Hamiltonian (equation 2.1) can be separated into an electronic and one nuclei part:

$$H_{el} = T_{el} + V_{nuc,el} + V_{el,el} + V_{nuc,nuc} \tag{2.1}$$

And the last term in the Hamiltonian, the potential energy $V_{nuc,nuc}$ of the nuclei, becomes a constant. The first Hohenberg-Kohn theorem states, that the ground state energy of a system is determined by its ground state electron density.[31] And the electron density is assesed in by the external potential of the nuclei acting on the electrons. If the true energy functional is known, the second Hohenberg-Kohn theorem even establishes a variation principle (equation 2.2). The energy of the real ground state density ρ is lower than the energy of any test density ρ_{test}:

$$E[\rho] \geq E[\rho_{test}] \tag{2.2}$$

Due to the poor performance of orbital-free DFT, Kohn-Sham DFT reintroduce orbitals to describe the electron density.[32] A trial density $n(r) = \sum_{i=1}^{N_{elec}} |\phi_i(r)|^2$ is build from Kohn-Sham orbitals $\phi_i(r)$. The Kohn-Sham-orbitals are described by a linear combination of basis set functions. The energy of the system is described by equation 2.3.

$$E_{DFT}[\rho] = T_S[\rho] + V_{KS}[\rho] \tag{2.3}$$

It is the sum of the kinetic energy T_S, calculated from a Slater determinant, and the Kohn-Sham potential V_{KS}.

The Kohn-Sham-potential, the effective single-particle potential, is in turn the sum of three parts:

$$V_{KS}[\rho] = V_{ne}[\rho] + J[\rho] + V_{xc}[\rho] \tag{2.4}$$

1. The potential energy of the external field of the nuclei acting on the electrons (V_{ne}).
2. The Coulomb functional J, which describes the electron-electron repulsion.
3. The exchange-correlation functional $E_{xc}[\rho]$, which contains the kinetic correlation energy, the potential correlation and exchange energy.

The second and third part both depend on the density. Therefore the trial density is used to build a Kohn-Sham-potential. Which in turn is then used to solve the Kohn-Sham equation (equation 2.5), where ϵ_i are the energies of the corresponding Kohn-Sham orbital ϕ_i.

$$[T + V_{KS}]\phi_i = \epsilon_i \phi_i \tag{2.5}$$

The Kohn-Sham orbitals are used to build a new electron density $n_{new}(r)$. If the difference between the old and the new trial density is below the convergence threshold, the iteration process is finished and the ground state density obtained. This process is called self-consistent field (SCF) method.

2.2. *Ab initio* Molecular Dynamics

The general procedure of Born-Oppenheimer Molecular Dynamics (BOMD) simulations is shown in figure 2.1a.

First, an initial configuration of the system is given by the user. It needs to contain the initial positions of the atoms in the system and additionally information about periodicity and the mean kinetic energy. The initial velocities of the system are assigned randomly and scaled in a way that the total momentum of the system is zero and that the mean kinetic energy has the desired value. The temperature for each atom can be computed via the equipartition principle ($\frac{1}{2}m\langle v_i^2\rangle = \frac{1}{2}k_BT$) as described in section 2.4 and rescaled if necessary.

The electronic ground state energy of the system is computed with density functional theory (DFT), described in section 2.1.[31, 32] Molecular dynamics simulations using quantum mechanical *ab initio* methods to compute the energies for the systems are called *ab initio* molecular dynamics (AIMD). The next step is then to calculate the forces acting on the atoms. This is done by using the Hellmann-Feynman theorem (equation 2.6).[33]

$$F_I = -\frac{\partial E_{DFT}(R_I)}{\partial R_I} \tag{2.6}$$

The Hellmann-Feynman force is the derivative of the total ground-state energy with respect to the nuclei coordinate. The energy is the eigenvalue of the Hamiltonian and can be described as such: $E = \langle\Phi_i|H|\Phi_i\rangle$. Only the electron-electron and nucleus-nucleus term of the Hamiltonian contribute to the differential of the total energy.

These Hellmann-Feynman forces are used to solve Newton's equations of motion for each atom I with mass m_I (equation 2.7).

$$F_I = m_I\frac{d^2R_I}{dt^2} \tag{2.7}$$

This second order differential equation is not trivial to solve due to the many-body nature of an MD simulation. The force and the acceleration of one atom depend on all other atoms and thus their time dependence is complex. The force can be obtained from the DFT calculations and the Verlet-algorithm is designed to solve this problem of the time-dependence of the acceleration.[34, 35] A Taylor expansion of the position R(t) gives equations 2.8 and 2.9, where R(t), v(t) and a(t) are the position, velocity and acceleration at time t and Δt is the timestep of the calculation.

$$R(t+\Delta t) = R(t) + \Delta t \cdot v(t) + \frac{1}{2}\Delta t^2 \cdot a(t) + \ldots \tag{2.8}$$

$$R(t - \Delta t) = R(t) - \Delta t \cdot v(t) + \frac{1}{2}\Delta t^2 \cdot a(t) - \dots \quad (2.9)$$

The sum of equations 2.8 and 2.9 truncated after the second order term give equation 2.10.

$$R(t + \Delta t) = 2R(t) - R(t - \Delta t) + \Delta t^2 \cdot a(t) \quad (2.10)$$

This integration scheme allows the computation of the positions of the atom at the next time step, which is continued until a sufficiently long trajectory has been computed.

BOMD describe the time evolution of a system with N particles in a volume V. And they remain constant, as does the constant of motion, the total energy E. The system described is microcanonical (constant NVE). But it is also possible to use MD for simulations of other ensembles, such as a canonical (constant NVT) or isothermal-isobaric ensemble (constant NPT). MD simulations of a canoncial ensemble for example can be obtained by employing different thermostats, which either use Monte Carlo moves (Andersen-thermostat) or use extended-Lagrangian equations of motion (Nos*é*-Hoover thermostat).[36–38] The third option are velocity rescaling thechniques, as in the CSVR thermostat.[39] CSVR is short for canonical sampling through velocity rescaling and the velocities are rescaled by a factor, that is computed on the fly by means of stochastic equations, so that the average temperature and its fluctuations are correspond to those of the canonical ensemble.

2.3. Programs and Settings

All *ab initio* molecular dynamics simulations have been carried out with the CP2K program package (version 2.4).[40] Periodic boundary conditions were applied for all calculations with a box size of 12.26 Å, 12.74 Å, and 14.41 Å in x-, y-, and z-direction, respectively. The x- and y-directions are determined by the size of the graphene sheet composed of 60 carbon atoms. The z-direction was determined by Cicero et al. using classical molecular dynamics simulations.[26] They used classical MD simulations to obtain the optimum distance for planar confinement of 54 water molecules between two graphene sheets, so that the stress along the z-direction reached a pressure equal to atmospheric pressure.

The equations of motion were integrated using a time step of 0.2 fs for all BOMD simulations. To allow for this time step, D_2O instead of water was used. For simplicity, the heavy water will also be referred to as water or H_2O hereafter. Hydrogen and deuterium will be used synonymously. The electronic structure calculations and the calculations for the forces in the BOMD simulations use density functional theory implemented in the QUICKSTEP code of CP2K.[31, 32, 41] The exchange and correlation functional in the generalized gradient approximation (GGA) by Perdew, Burke and Ernzerhof (PBE) was used.[42] QUICKSTEP uses the Gaussian and plane wave method (GPW) to describe the electronic interactions.[43] A dual basis set of atom centered Gaussian orbitals and plane waves is used. This dual approach allows the use of the advantages of both types of basis functions.

In the GPW method only valence electrons are treated. The interaction of the valence electrons with the nuclei and core electrons is described by pseudopotentials. The pseudopotentials of Goedecker, Teter and Hutter (GTH) were used, which are already included in the CP2K program package.[44–46] The valence pseudo-wavefunctions are expanded with a Gaussian-type basis set and are used to calculate the electronic kinetic energy and the electronic interactions with the ionic cores. The electron density in reciprocal space is represented by an auxiliary basis set of plane waves. They are used to compute the electronic Hartree energy and the exchange-correlation energy in reciprocal space and then fast-Fourier transformed (FFT) to get the real-space representation.[47] The integration of the plane waves is performed on a grid of k-points. Six multigrids were used with a cutoff energy of 300 Ry. A triple-ζ basis set with two sets of polarization functions (TZV2P) was used as a Gaussian type basis set together with the auxiliary plane wave basis set implemented in CP2K.[48, 49]

The individual systems that were chosen will be explained in greater detail later in section 3. The temperature was controlled via canonical sampling through velocity rescaling (CSVR thermostat) with a coupling time of 50 fs.[39] Since the temperature of the system evolved slowly, 2 ps of Langevin-dynamics were employed ($\gamma = 0.1 fs^{-1}$).

After equilibration, all four systems were simulated as a microcanonical ensembles (NVE constant). Total simulation times are reported in table 2.1.

Table 2.1.: Total simulation times of the systems.

System	Number of Steps	Simulation Time [ps]
1	100000	20.00
2	84200	16.84
3	68600	13.72
4	100000	20.00

The relatively high simulation temperature of 380K in the equilibration runs and production runs was necessary due to the neglect of quantum motion of hydrogen/deuterium in water in MD simulations.[50, 51] To obtain diffusion behavior and structures comparable to water at room temperature, the simulation temperature needs to be increased by about 100K. Schwegler *et al.* even found a simulation temperature of 415 K for BOMD of water to obtain the diffusion behavior observed experimentally at room temperature.[51] Since our simulation temperature is lower, the diffusion behavior and structural behavior of the simulated water is slightly below room temperature.

2.4. Temperature Development

The temperature development of the different atom species during the equilibration was monitored. This was necessary, as the simulations started from a flat and therefore low temperature configuration of graphene. CP2K only monitors the temperature of the system as one. The equilibration was continued until the graphene sheets and the water roughly had the desired temperature of 380 K.

Velocity is defined as the distance covered in a specific time interval (equations 2.11, 2.12, and 2.13). The trajectory file of the MD simulation gives the positions of all atoms after every time step, therefore the velocity is the distance covered by the atoms divided by the time step of the calculations (Δ t=0.2fs).

$$v_x(t) = \frac{x(t+\Delta t) - x(t)}{\Delta t} \tag{2.11}$$

$$v_y(t) = \frac{y(t+\Delta t) - y(t)}{\Delta t} \tag{2.12}$$

$$v_z(t) = \frac{z(t+\Delta t) - z(t)}{\Delta t} \tag{2.13}$$

The velocities were used to compute the average kinetic energies K_i for the different atomic species i (equation 2.14). Since there were four nitrogen atoms at most and due to the fact that the nitrogen atoms are a part of the graphene sheet, the nitrogen atoms were included in the statistics of the carbon atoms. Then the equipartition principle (equation 2.15) was solved for the temperature (equation 2.16). This was then done for every step and the results are shown in figure 3.3 in section 3.2.

$$K_i = \frac{1}{N_i} \sum_i^N \frac{1}{2} m(v_x^2 + v_y^2 + v_z^2) \tag{2.14}$$

$$K = \frac{3}{2} k_B T \tag{2.15}$$

$$T = \frac{2}{3} \frac{K}{k_B} \tag{2.16}$$

2.5. Mass Density Profiles

Density profiles give insight to the structures of systems at stationary points or throughout whole trajectories. The whole process is schematically shown in figure 2.2. It is assumed, that all atoms are point-like. Then the distance along which the profile is to be computed is divided into intervals or bins. Since we only computed density profiles along the z-direction, the intervals shall be named Δz. The systems are contained in an orthorhombic unit cell with periodic boundary conditions. The unit cell can thus be divided into volume slabs of the same size (equation 2.17, figure 2.3). These volume slabs are called bins which will be numerated with index b.

$$V_b = L_x \cdot L_y \cdot \Delta z \tag{2.17}$$

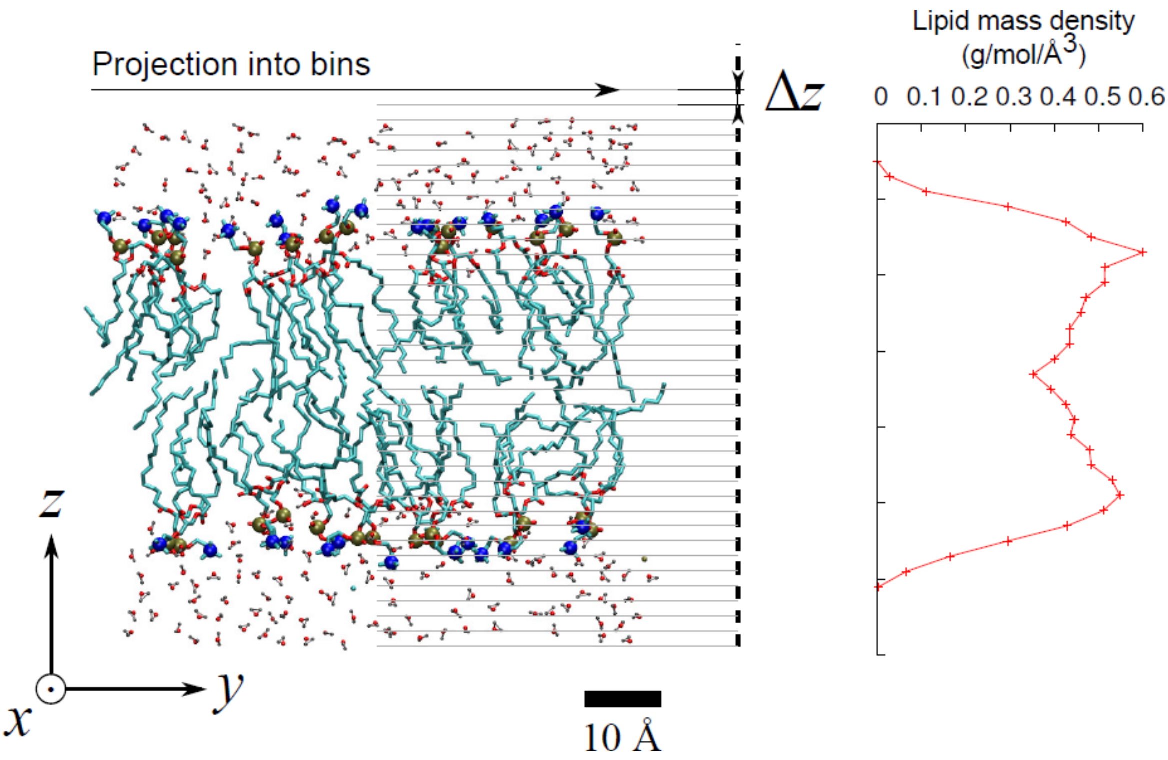

Figure 2.2.: Schematic representation of the calculation of a mass density profile. The system is prejected into bins (left) and the resulting density profile is displyed on the right hand side. Reprinted from Ref. [52] with permission from Elsevier.

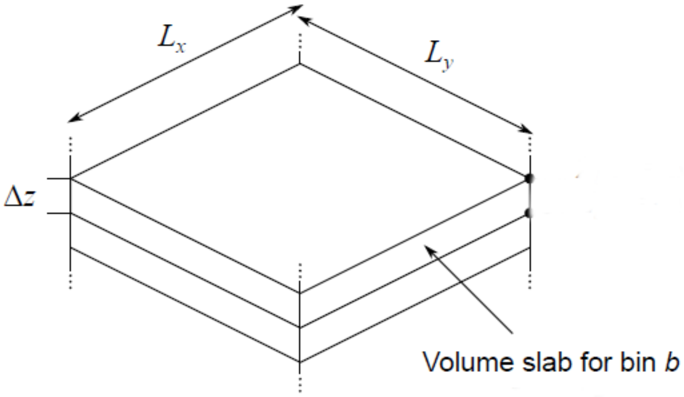

Figure 2.3.: Volume of the slabs for an orthorhombic unit cell with periodic boundary conditions.Reprinted from Ref. [52] with permission from Elsevier.

The density is computed as shown in equation 2.18. The number of atoms in each bin (N_{bin}) are counted. p_i is the atom property of interest, for example the number, mass, charge or electron number of the atoms. These computed densities can then be mapped to the z-direction, as shown in figure 2.2

$$\rho_b = \sum_{i}^{N_{bin}} \frac{p_i}{V} \tag{2.18}$$

The density profiles can also be computed for all steps of the trajectory to compute density averages.

2.6. Radial Distribution Functions

Another technique for structural characterization of MD simulations are radial distribution functions (RDF). The radial distribution function, or pair correlation function, is defined in equation 2.19.

$$g(r) = \frac{n(r)}{\rho V} = \frac{n(r)}{\rho \cdot 4\pi r^2 \Delta r} \tag{2.19}$$

The RDF is defined as the average number of neighbours of a particle as the function of the distance from said particle. It can be constructed in a similar fashion compared to the density profiles described in section 2.5. The volume around the chosen particle is divided into spheres with thickness Δr. The volume of the sphere is $V = \frac{4}{3}\pi(r + \Delta r)^3 - \frac{4}{3}\pi r^3$. Since Δr is quite small, the volume of the spheres simplifies to $V = 4\pi r^2 \Delta r$. The number of particles in the sphere $n(r)$ is counted, divided by the mean density of particles in the system and the volume of the sphere V. This is not only done for a single particle in the system, but for all particles of the same type and sampled over the whole trajectory to obtain a statistically meaningful ensemble average.

2.7. Hydrogen Bonding

The hydrogen bonds in the systems were analyzed using a novel machine learning procedure implemented in PAMM (probabilistic analysis of molecular motifs) software package.[53] The process for the evaluation of the hydrogen bonds is shown schematically in figure 2.4. The procedure consists of the following steps (for simplicity the dimension is reduced to two):

(a) First, three distances for each combination of three atoms are calculated: $\nu_i = d(td_i - th_i) - d(ta_i - th_i)$ defines the difference in the distances between the hydrogen bond acceptor and the hydrogen atom, and the hydrogen bond donor and the hydrogen atom. $\mu = d(td - th) + d(ta - th)$ is the sum of the two distances and $r = d(td - ta)$ the distance between the hydrogen bond donor and acceptor. The three distances define the geometry of the hydrogen bond. The

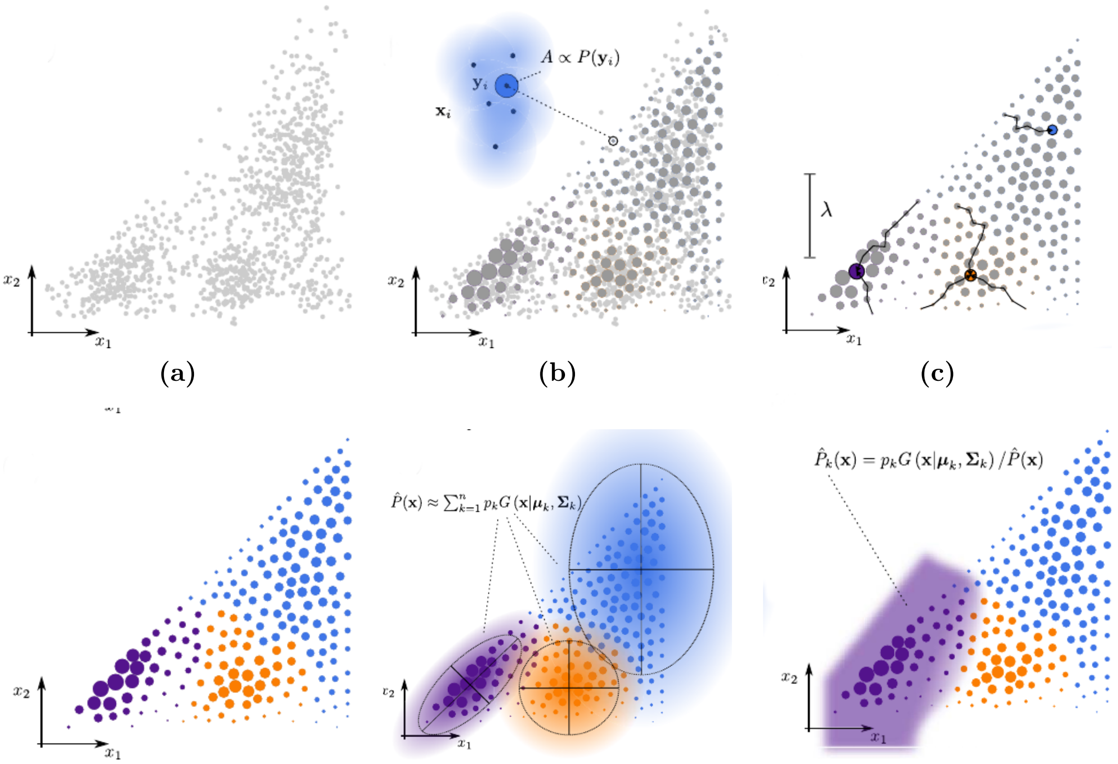

(a) (b) (c)

(d) (e) (f)

Figure 2.4.: The schematic representation of the procedure the program package PAMM uses to analyze hydrogen bonding in molecular dynamics simulations.[53](Reprinted with permission from Gasparotto *et al.*, *Journal of Chemical Physics* **141**, 174110. Copyright 2014, AIP Publishing LLC.)

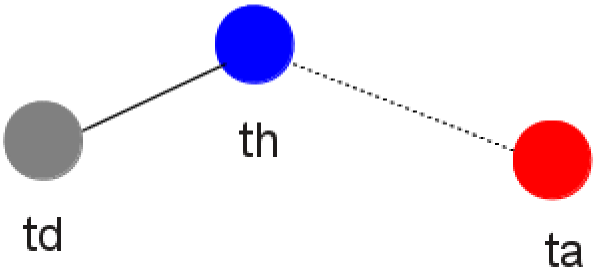

Figure 2.5.: Triplet of atoms that can form a hydrogen bond (dashed line). ta is the hydrogen bond acceptor, td the donor and th the hyrdogen bonded hydrogen atom.

distances are computed for each possible combination i of three atoms which are able to form a hydrogen bond. In water this could be two oxygens and one hydrogen atom. But the hydrogen bond acceptor could also be a nitrogen atom in the case of the nitrogen-doped graphene surfaces. The three distances are denoted as vector χ.

(b) The structural data vectors χ are distributed very irregularly, making it difficult to analyze them and to find probability distributions. They are therefore collected into a grid of points. As depicted in figure 2.4b, the different dot sizes depict different numbers of structure vectors χ collected into one grid point. They are basically a twodimensional histogram. $\mathrm{P}(\mathrm{y}_i)$ is the density estimate for each grid point.

(c) In a third step, the maxima in the probability distribution, in other words the grid points with the highest density estimate P. Then, each gridpoint is assigned to a maximum of the probability distribution using a quick-shift procedure (figure 2.4c). The procedure follows the paths to the nearest maximum and assign all grid points to this probability mode. This is done until all grid points have been assigned to a probability cluster.

(d) The three clusters that were identified by the quick-shift procedure are shown in figure 2.4d. Since the assignment is only based on probabilities and not hard definitions of structural parameters, the assinment to the clusters is very flexible.

(e) Each cluster is then fitted with a Gaussian mixture model to define the probability distribution within the cluster (figure 2.4e).

(f) The cluster of the structural parameters associated with hydrogen bonding is the purple cluster shown in figure 2.4f. As mentioned before, the definition of the hydrogen bond parameters is based on probabilities of recurring structural patterns and is therefore very fuzzy and flexible.

At the end this produces a histogram of the average number of hydrogen bonds the three atoms engage in.

The autocorrelation function $f(t) = \langle s(t=0)s(t) \rangle$ defines the time evolution of the hydrogen bonds, with s being the number of hydrogen bonds at time t.

3. Results and Discussion

3.1. Systems

Four systems were selected to investigate the interaction of water with nitrogen-doped graphene surfaces. All systems are composed of a graphene layer of 60 carbon atoms and 54 water molecules. Periodic boundary conditions apply in three dimensions. The size of the simulation box in x- and y-direction is determined by the graphene sheet and has a dimension of 12.26 Å and 12.75 Å, respectively. The box size in z direction is 14.41 Å. This distance has been determined by Cicero *et al.* to be the distance where 54 water molecules are confined at atmospheric pressure.[26] The starting configuration for the undoped graphene surface is shown in figure 3.1.

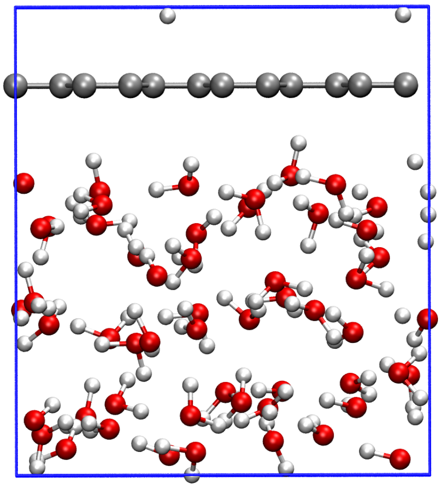

Figure 3.1.: System 1, graphene layer of 60 carbon atoms and 54 water molecules inside the orthorhombic simulation box (blue).

The four systems chosen are:

- **System 1: Graphene**

  The first system chosen was an undoped graphene surface (Figure 4.1a). This allows comparison with the work of Cicero *et al.*, to determine if the system behaves according to their calculations. The comparison is necessary since a different approach to solving the electronic problems with the GPW method is used. It also allows for comparison between the undoped surface with the nitrogen-doped surfaces with the same computational setup. This comparison

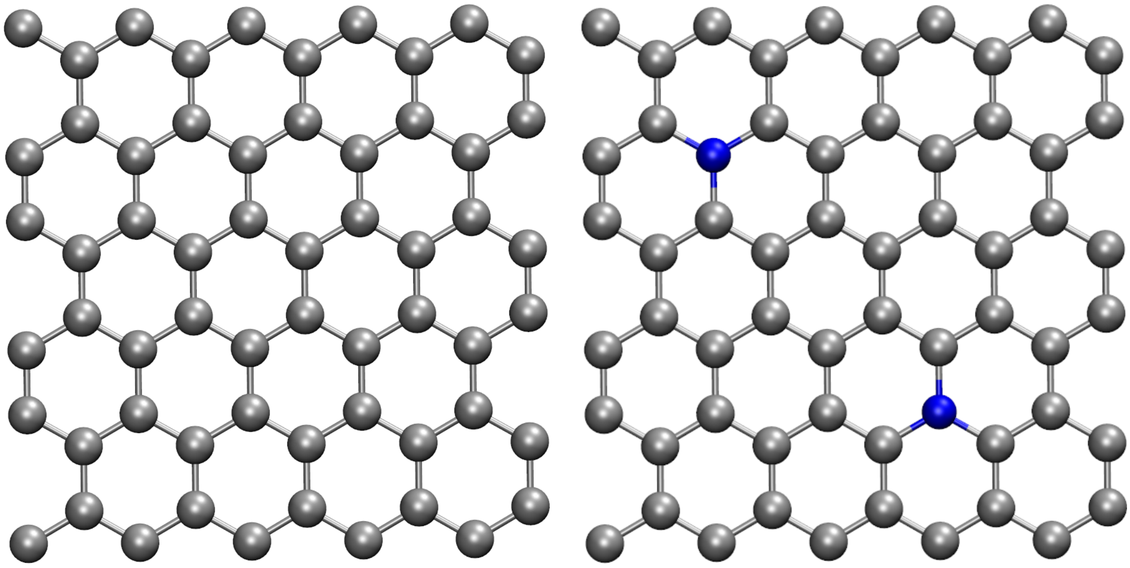

(a) System 1 **(b)** System 2

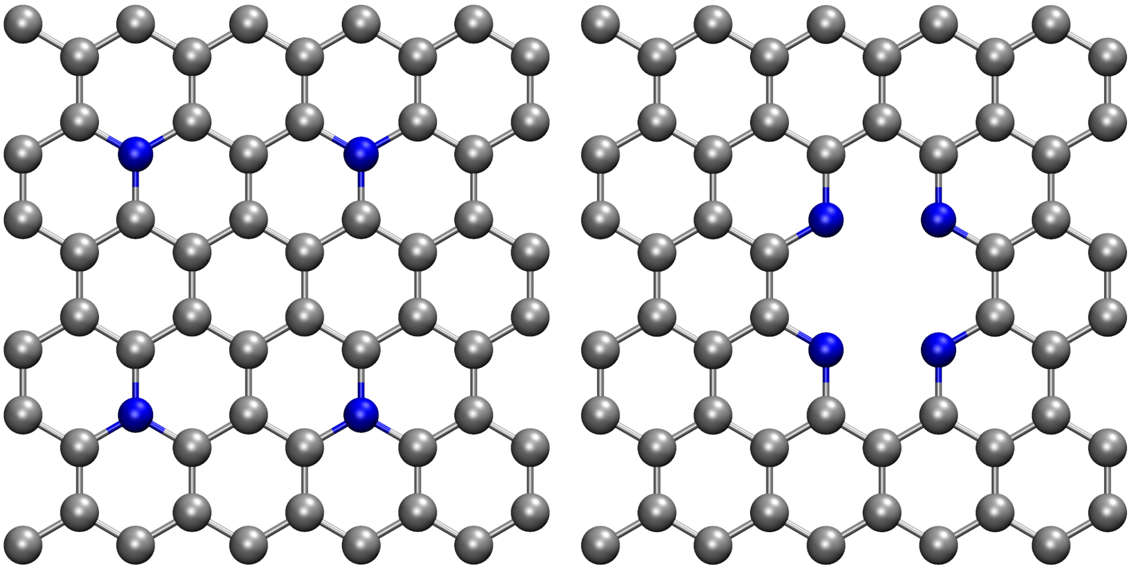

(c) System 3 **(d)** System 4

Figure 3.2.: nitrogen substitution patterns of graphene surface of 60 carbon atoms (a)pure, undoped graphene surface, (b) substitutional nitrogen defect, 2N (c)substituional nitrogen defect, (d) pyridine-type defect with divacancy, 4N

is useful, since the pure graphene surface did not show any catalytic activity in the OER in the experiment.[15]

- **System 2: 2 N - Substitutional**

  The second system system contains two nitrogen atoms in a substitutional nitrogen pattern (Figure 4.1b). According to the calculations by Fujimoto and Saito, the substitutional nitrogen defect is the most stable and energetically most favorable of all investigated nitrogen defects.[23] This substiutional nitrogen defect was observed in the catalytic active nitrogen-doped graphene surfaces and about 37% of the nitrogen atoms in the surface were measured to be bound in this structure.[15] The experimental nitrogen concentration was measured to be 4.1%. The nitrogen concentration in the second system is slightly lower with 3.3%.

- **System 3: 4 N - Substitutional**

  The third system is shown in figure 4.1c and contains four nitrogen atoms in the substiutional pattern. It has a higher nitrogen concentration with 6.7% but also in the most stable substitutional pattern.

- **System 4: Tetramerized Pyridine-Type**

  System 4 is shown in figure 4.1d and also contains four nitrogen atoms. These however are arranged in a pyridinic structure around a divacancy. According to Fujimoto *et al.*, the substitutional pattern is the most stable nitrogen-doped structure. But upon the presence of vacancies, pyridine-type structures are more likely to form. The most stable structures are the trimerized pyridine-type defect around a monovacancy (figure1.4g) and the tetramerized pyridine-type structure around the divacancy (figure 1.4h). Both structures have a similar formation energy and divacancies are easier to generate in graphene. Additionally, the tetramerized structure was chosen due to the same number of nitrogen atoms contained as in system 3.

Starting from a flat graphene sheet, all four systems were equilibrated as described in section 3.2 and later simulated in the microcanonical ensemble (constant number of particles, volume and energy) to calculate unbiased structural properties and to probe water dynamics, avoiding artifacts arising from the use of thermostats.

3.2. Equilibration

The four systems were equilibrated by performing *ab initio* MD simulation in the canonical ensemble (NVT constant) at a temperature of 380 K. The temperature for each step was calculated as described in section 2.4 and the temperature evolution for each system is reported in figure 3.3. To achieve homogeneous equilibration of all the degrees of freedom of the system a local Thermostat (Langevin) was used for two ps and the equilibrations were completed using the CSVR thermostat. The equilibration times are reported in table 3.1.

Table 3.1.: Overview over all equilibration runs. The first column displays the system number, the second column the number of nitrogen atoms in the system and the third column the substitution pattern of the nitrogen atoms. The fourth column displays the simulation time for the equilibration with Langevin dynamics in ps and the last column displays the total simulation time in ps for each system.

System	# N	Substitution Pattern	Langevin time [ps]	Total time [ps]
1	0	-	1.64	10.02
2	2	substitutional	2.06	13.00
3	4	substitutional	1.94	11.00
4	4	pyridine-type	2.10	10.14

Since the simulations were started from a flat graphene sheet optimized at 0 K, the initial temperature for the carbon atoms is very low. Graphene sheets at higher temperatures exhibit ripples. The starting structures were taken from simulated structures of Cicero *et al.*. Their simulation temperature for the water was 400K. The cold graphene surface and the warm water molecules therefore needed to be equilibrated to the desired simulation temperature of 380 K.

3.3. Structure of Water at Nitrogen-doped Graphene Surfaces

First, to visualize the effect of the nitrogen atoms on the water molecules qualitatively, the trajectory was sampled every 20 fs within 2.5 Å of the surface. The results are shown in figure 3.4.

For the undoped graphene surface in system 1, only a few oxygen atoms from the first interfacial layer are visible. The deuterium atoms displayed are part of the molecules pointing at the surface. They show no preference for any atoms withing the pristine graphene surface and are evenly distributed. The snapshots of the water molecules of the second system also show an even distribution. The substiutional nitrogen atoms have no effect on the deuterium atoms of the first interfacial layer. The four substitutional nitrogen atoms in the third system also have no significant effect on the water atoms in the first interfacial layer.

Only the four pyridine-type nitrogen atoms affect the water layers significantly. The water not only points at the graphene surface with one O-D bond but also enters the exclusion volume above the divacancy and interacts with the nitrogen atoms.

To quantify this behavior, density profiles and radial distribution functions of the system were calculated. The density profiles for all four systems were computed as described in section 2.5 and are shown in figure 3.5.

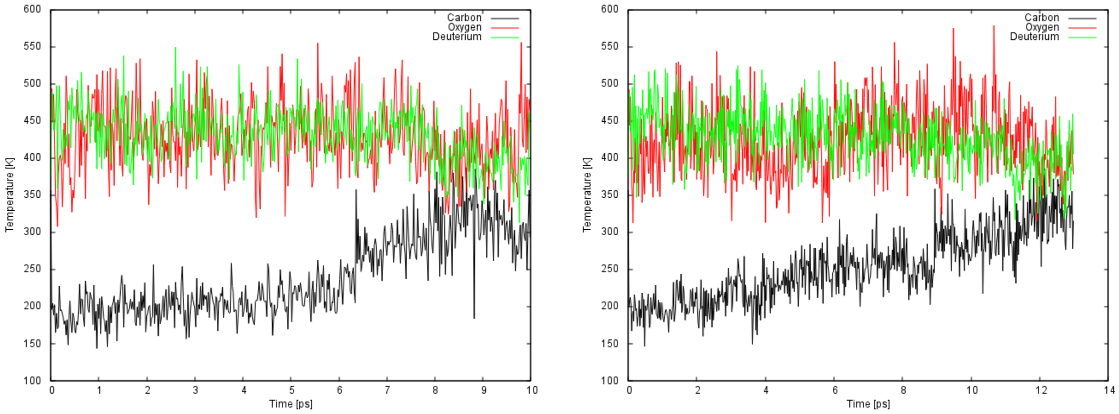

(a) System 1 **(b)** System 2

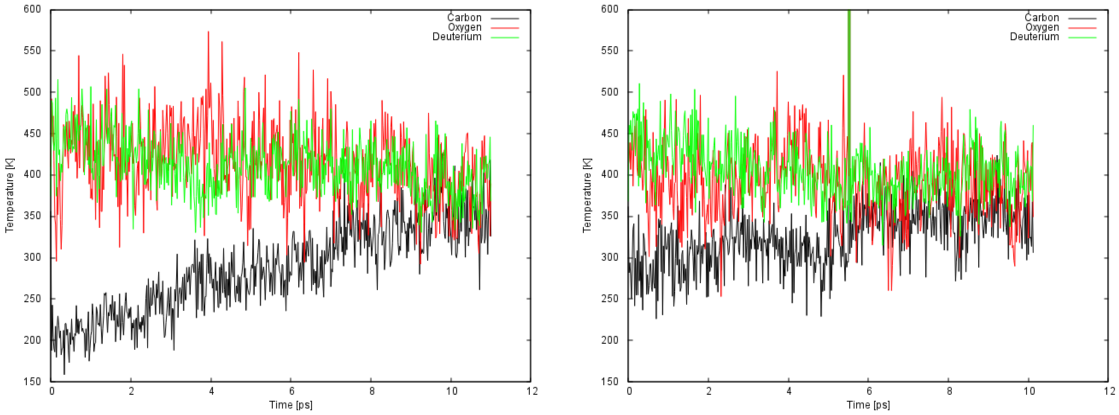

(c) System 3 **(d)** System 4

Figure 3.3.: Temperature development of atomic species during the equilibration. The nitrogen atoms were included in the statistics of the carbon atoms.

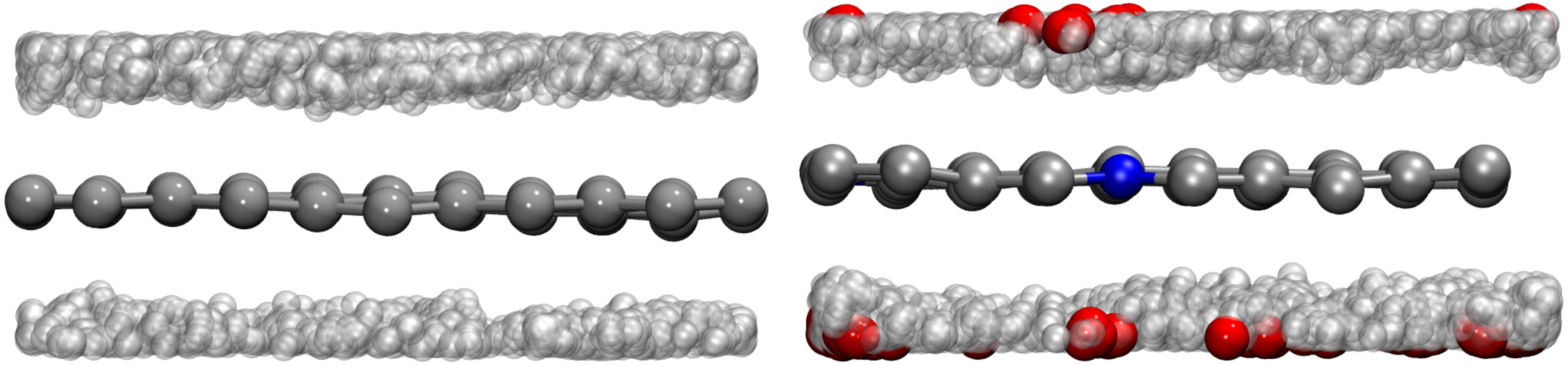

(a) System 1 **(b)** System 2

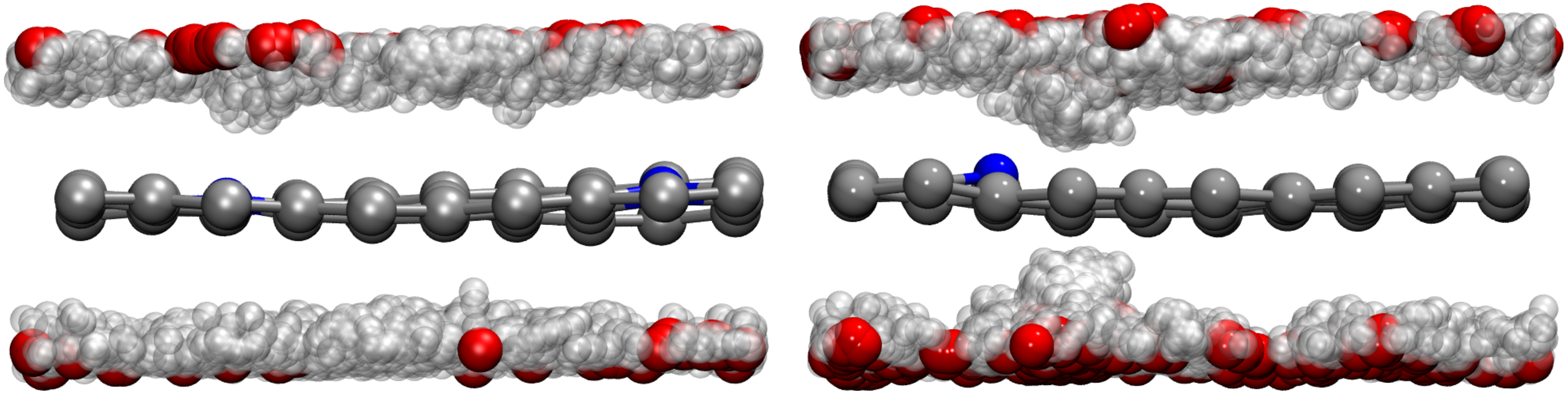

(c) System 3 **(d)** System 4

Figure 3.4.: Snapshots of oxygen and deuterium atoms within 2.5 Å of the undoped and doped graphene surfaces sampled every 20 fs.

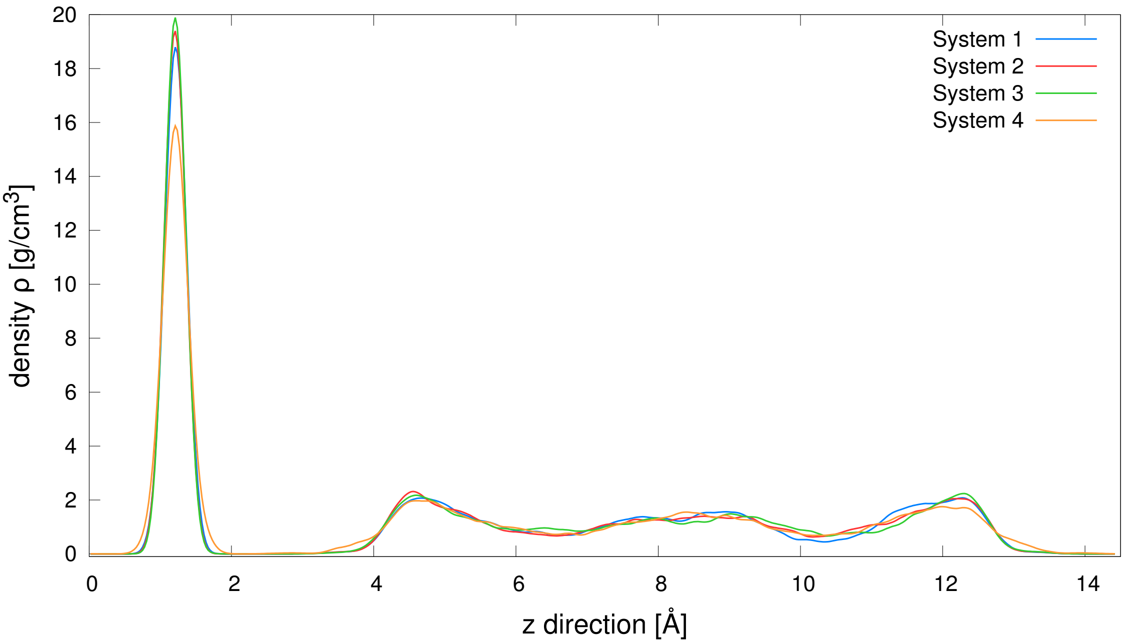

Figure 3.5.: Mass density profile in z-direction for all four systems after a simulation time of 20 ps.

The four systems all exhibit similar mass density profiles. All of them exhibit a high peak at about 1.2 Å originating from the doped and undoped graphene sheets. The height of the peak depends on the number of nitrogen atoms in the surface and the substitution pattern of the surface. Systems 1, 2 and 3 have no vacancies and are doped with zero, two and four nitrogen atoms respectively. Due to the increasing number of nitrogen atoms in the graphene sheet, the density increases from 18.8 to 19.9 g/cm^3. System four is also doped with four nitrogen atoms. But due to the divacancy the density for the graphene sheet is significantly lower than for the other three systems (15.9 g/cm^3). Another difference is the width of the peaks originating from the graphene sheets. The peak for system four is

Between the water and the graphene sheet, there is an exclusion volume of about 2.5 Å. This is not only consistent with the calculations of Cicero et al. studying water confined between graphene sheets, but also with other systems studied.[26] After the exclusion volume two interfacial layers can be observed with a density above bulk density (1 g/cm^3). The density of the interfacial layer rises to about 2 g/cm^3. In between the two interfacial layers is a third layer whose density oscillates around bulk value. While the peaks for the interfacial layers of the undoped surface (System 1) and the two substitutional doping patterns (Systems 2 and 3) rise sharply, the pyridinic system 4 shows a shoulder. This indicates stronger interactions of water with the surface and therefore the density profiles of the water were looked at more closely.

The density profiles of oxygen and deuterium were computed separately and are shown in figure 3.6.

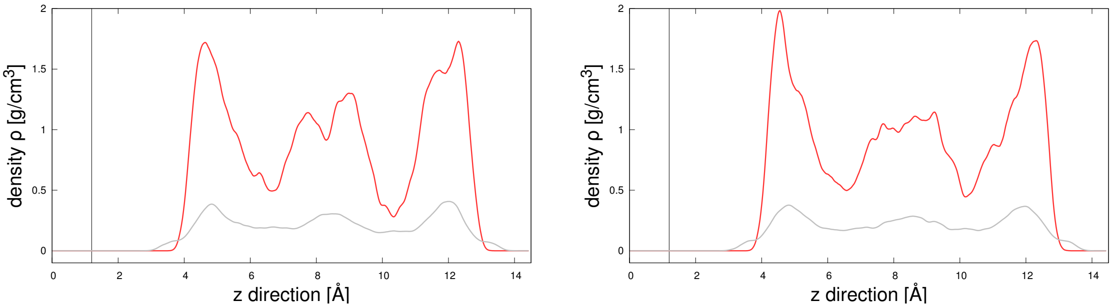

(a) System 1 **(b)** System 2

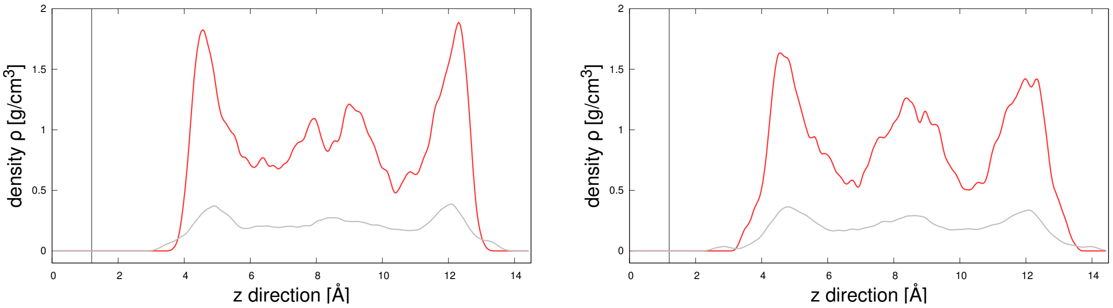

(c) System 3 **(d)** System 4

Figure 3.6.: Mass density profiles of oxygen atoms (red) and deuterium atoms (grey) in all four systems over a simulation time of 20 ps. The vertical black line marks the mass density maximum of the respective graphene surfaces.

The density profiles for deuterium and oxygen all systems are quite similar again. The oxygen and hydrogen profile also display the exclusion volume and the rise in density in the interfacial layers. In all four systems, a small shoulder in the deuterium curve can be seen. This indicates a tendency for some OD-bonds from the interfacial layer water molecules to point at the graphene surface. These water molecules are still within the interfacial layer though. The density profile for system 4 differs from the rest. The deuterium curve not only displays a shoulder but a distinct bump. This bump is also closer to the surface by about 1 Å. The oxygen curve also shows a shoulder for system 4 unlike for all other systems. This means that the water molecules not only point one OD-bond toward the surface, but also leave the interfacial layer structure to interact with the tetramerized pyridine-type defect structure in system 4.

Another technique to quantify structures in MD trajectories are radial distribution functions, as described in section 2.6. Radial distribution functions quantify the distance of atoms with respect to one another. Different radial distribution functions for different types of atom pairs were computed.

Figure 3.7 shows the radial distribution functions for the four systems of the atom types contained in the water molecules. Figures 3.7a, 3.7b, and 3.7c show the radial distribution function between deuterium and deuterium, oxygen and oxygen, and oxygen and deuterium, respectively.

The deuterium-deuterium RDF shows a large peak at about 1.5 Å. This peak originates from the other deuterium bound to the oxygen atom in a water molecule. The second peak at 2.5 Å can be attributed to the first hydrogen bonded coordination sphere. These hydrogen bonded atoms are also the cause of the peak in the oxygen-oxygen RDF at 2.8 Å. The high peak in the oxygen-deuterium RDF at 1 Å originates from the two deuterium atoms bonded to the oxygen in the water molecule. The smaller peaks at 1.8 Å and 3.5 Å are caused by the first and second hydrogen bonded coordination sphere.

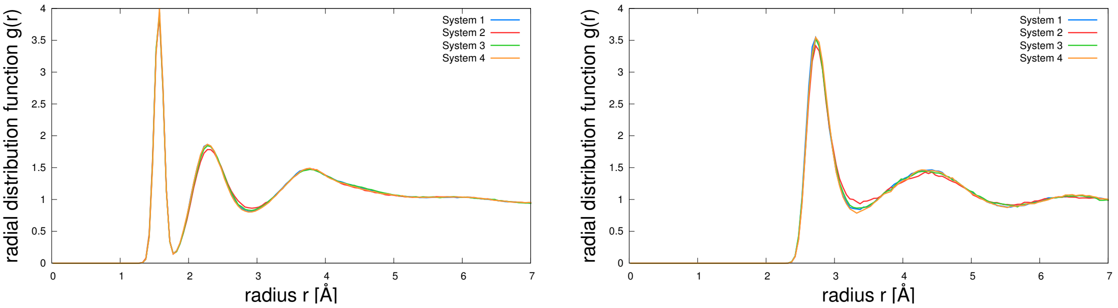

(a) HH **(b)** OO

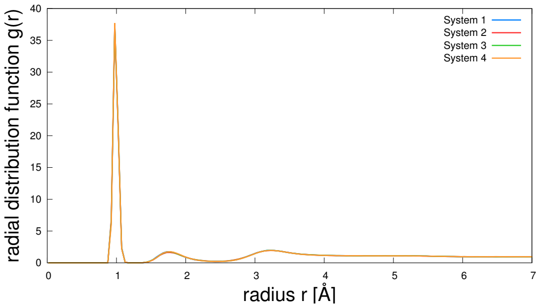

(c) OH

Figure 3.7.: Radial distribution functions of all four systems between (a) deuterium and deuterium, (b) oxygen and oxygen, and (c) oxygen and deuterium.

All three radial distribution functions are similar for all of the four systems. The nitrogen-doping does not change the behavior of the confined water as such and only has a local effect on the interfacial layer.

A comparison of the RDFs of system 4 with bulk water are shown in figure 3.8. MD simulations of the bulk water were also carried out with CP2K using the PBE functional and the same basis set, but using a slightly lower simulation temperature of 300 K.

The RDFs differ slighlty in amplitude but not significantly in their form otherwise. The peaks described above still occur at the same distances. The bulk structure is more ordered. The reason for this effect is the confinement of the water between the graphene sheets.

Of more interest are the radial distribution functions between nitrogen and oxygen (figure 3.9c), nitrogen and deuterium (figure 3.9d), carbon and oxygen (figure 3.9a), and carbon and hydrogen (figure 3.9b). The curve for the radial distribution function

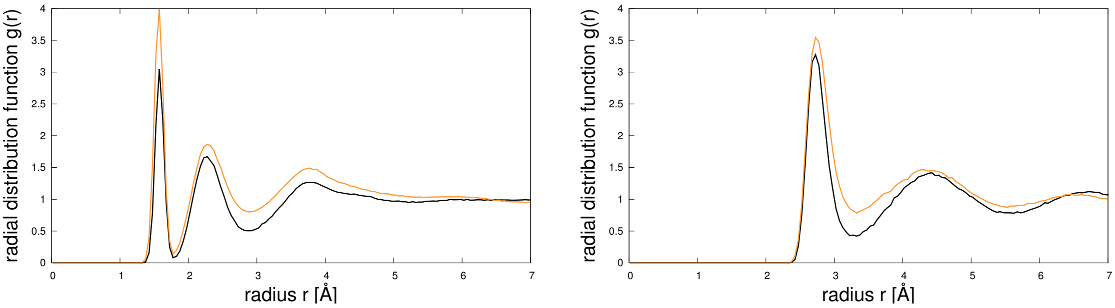

(a) HH **(b)** OO

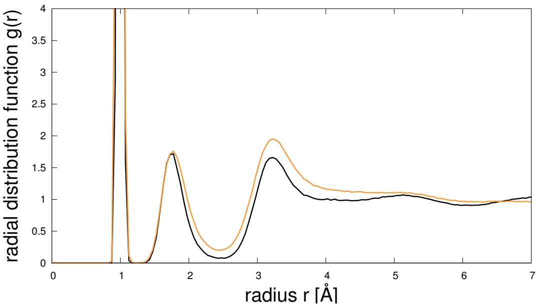

(c) OH

Figure 3.8.: Radial distribution functions of bulk water (black) and system 4 (orange) between (a) deuterium and deuterium, (b) oxygen and oxygen, and (c) oxygen and deuterium.

between carbon and oxygen begins to rise sharply at about 3 Å and then flattens. This can be attributed to the oxygen atoms in the bulk water and no significant interaction between the oxygen and carbon atoms. The radial distribution of carbon and hydrogen looks similar. A small shoulder between 2 and 3 Å can be attributed to the O-D bonds pointing at the surface once again. But also no significant interaction between the carbon atoms and hydrogen atoms can be seen.

Due to the small number of nitrogen atoms in the systems, the curves for the radial distribution functions computed with the nitrogen atoms are not very smooth. They display a significant difference in behavior compared to the radial distribution functions of the carbon atoms though. For systems 2 and 3, containing two and four substituional nitrogen atoms, the radial distribution functions for nitrogen with oxygen and deuterium look similar to those of carbon. System four, featuring the four pyridine-type nitrogen atoms around the divacancy, does not display that behavior. The radial distribution function between nitrogen and oxygen shows a maximum at a distance of about 3 Å. Maxima in RDFs indicate binding, and since the peak is at a similar distance as the peak in the OO-RDF (figure 3.7b), this peak can be attributed to hydrogen bonding between the water and the pyridine-type nitrogen atoms in the surface. This is underlined by the radial distribution function between nitrogen and deuterium. It begins to rise sharply at about 1.5 Å, as compared to the 2.5 Å of the other two systems. The typical hydrogen bond length is about 2 Å.

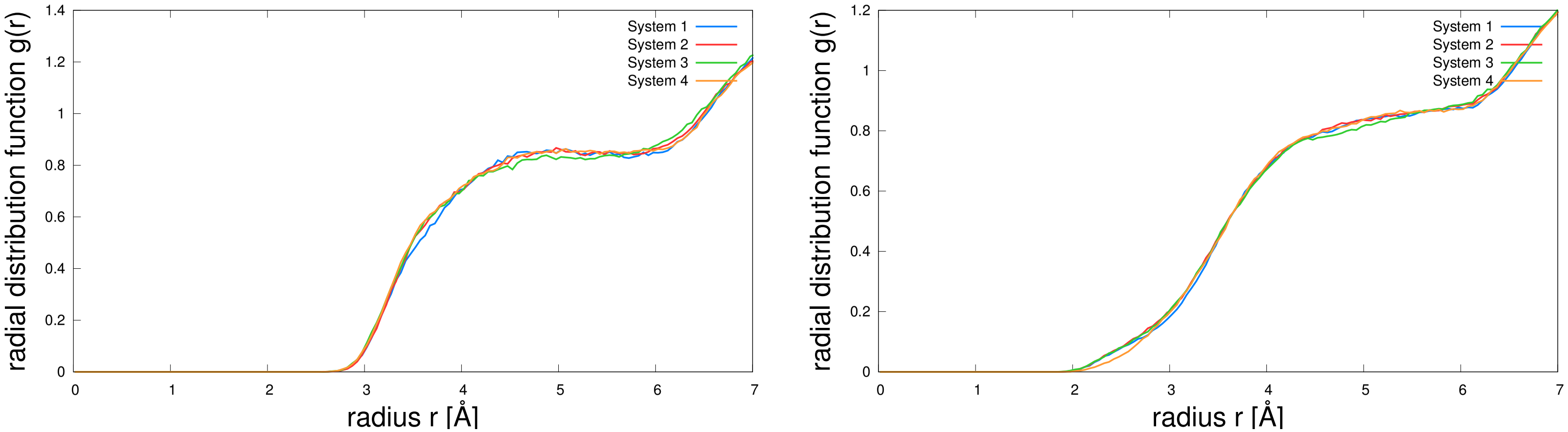

(a) CO **(b)** CH

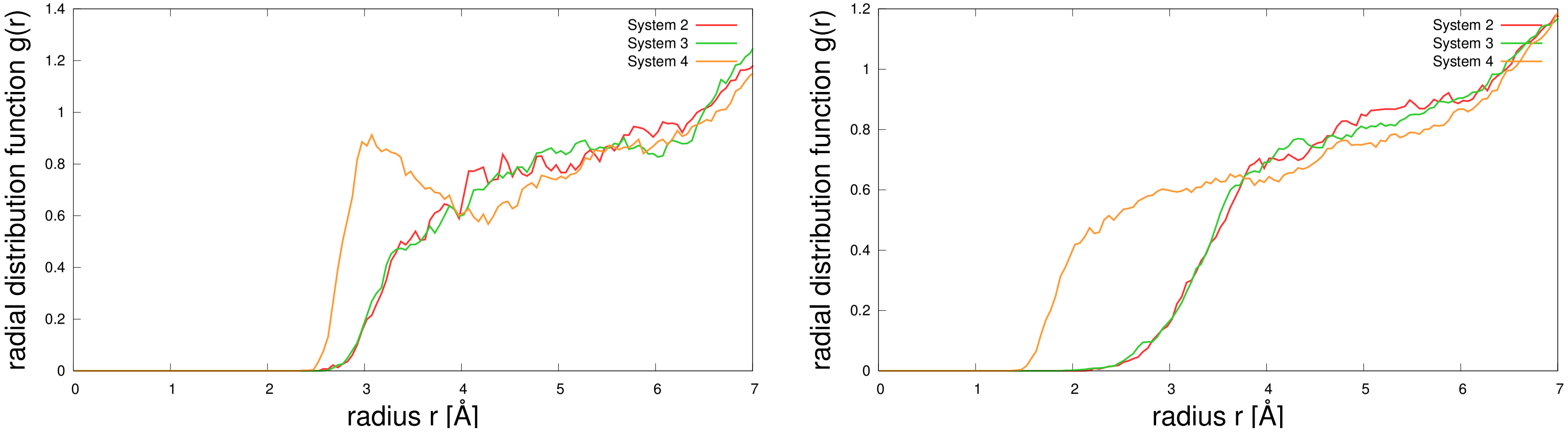

(c) NO **(d)** NH

Figure 3.9.: Radial distribution functions of the systems between (a) carbon and oxygen atoms, (b) carbon and hydrogen atoms, (c) nitrogen and oxygen atoms, and (d) nitrogen and hydrogen atoms.

3.4. Hydrogen Bonding

Since both the density profiles and the radial distribution functions suggest hydrogen bonding between the pyridine-type defects in system 4 and the water molecules, hydrogen bonding in all four systems was examined in detail, extracting the details of the electronic density. The hydrogen bonds were computed using the pamm package by Gasparotto *et al.* as described in section 2.7.[53]

First the hydrogen bonds in the water were analyzed. The histograms for the hydrogens to be engaged in a hydrogen bond between two oxygen atoms are shown in figures 3.10a to 3.10d. In all four systems, most of the hydrogen atoms engage in one hydrogen bond inside the water bulk. However, there is a distinct peak, showing that 4 % of the hydrogen atoms do not engage in hydrogen bonding in the water bulk. These hydrogen atoms either point toward the surface or might engage in hydrogen bonding with the nitrogen atoms in the surface.

These broken hydrogen bonds are also visible in the histograms of the oxygen atoms (figures 3.10e to 3.10h). There are slightly more acceptor oxygen atoms than donors. The molecules with the dangling O-D bonds only accept hydrogen bonds and can form only one hydrogen bond in return.

Since PAMM can not only recognize hydrogen bonds between water molecules but every atom of interest, the hydrogen bonding between the water layer and the nitrogen atoms in the doped graphene surfaces were analyzed. The interaction with the carbon atoms is very weak and did not give any results. Even analyzing the hydrogen bonding between the water molecules and the nitrogen atoms proved very difficult due to the low number of nitrogens and the weak bonding. A very fine grid of 2500 points and a longer trajectorywas necessary to obtain results at all. For the analysis of hydrogen bonding in water only 1000 grid points and every 100th step were necessary to obtain meaningful results.

The histograms for the hydrogen bonding between water and the nitrogen atoms are shown in figure 3.11. In sytem 2 (figure 3.11a) almost none of the two substitutional nitrogen atoms ever engage in hydrogen bonding at all. System 3 (figure 3.11b) shows a very weak tendency for some of the four substitusional nitrogen atoms to engage in hydrogen bonding. This is a very rare occurence, which suggests that the hydrogen bonds are very weak. System 4 contains four pyridine-type nitrogen atoms, which in contrast engage in hydrogen bonding quite often (figure 3.11c). The peak of the histogram is below one hydrogen bond, still suggesting a weak hydrogen bond. But the nitrogen atoms are often hydrogen bonded and the broadness of the histogram indicates weak hydrogen bonds that continuiously broken and formed again.

Additionally to the probability analysis of the hydrogen bonding, the dynamics of the hydrogen bonding in systems 3 and 4 were investigated. Figure 3.12 shows the time autocorrelation function as defined in 2.7 for both of the systems.

The decay in the correlation time of hydrogen bonds between water and nitrogen is much than for the bulk hydrogen bonds in water for both systems. This indicates more dynamics in the system, the hydrogen bonds with nitrogen are broken much faster than with the other water molecules in the system. The short correlation times

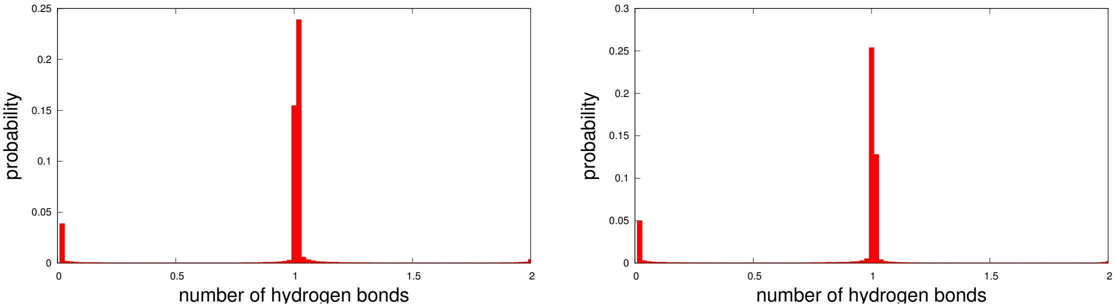

(a) System 1 - hydrogen **(b)** System 2 - hyrdogen

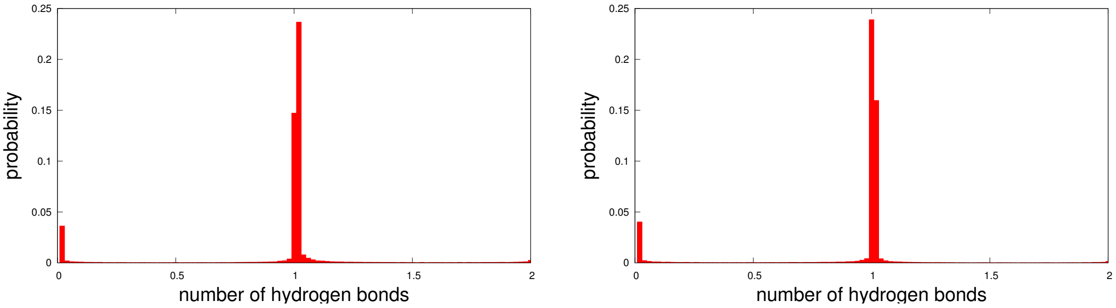

(c) System 3 - hydrogen **(d)** System 4 - hydrogen

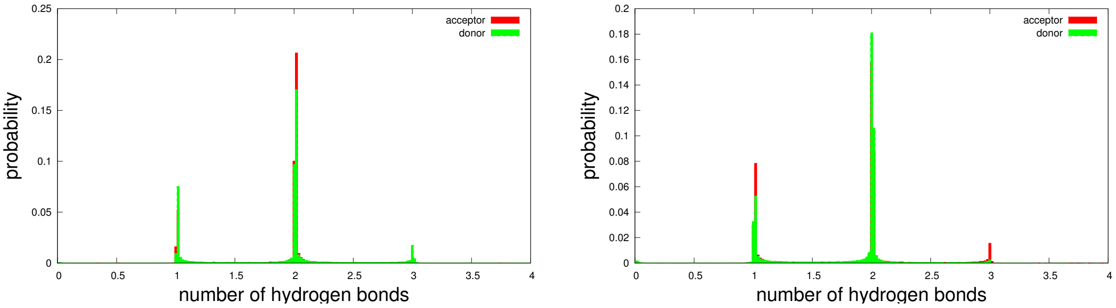

(e) System 1 - oxygen **(f)** System 2 - oxygen

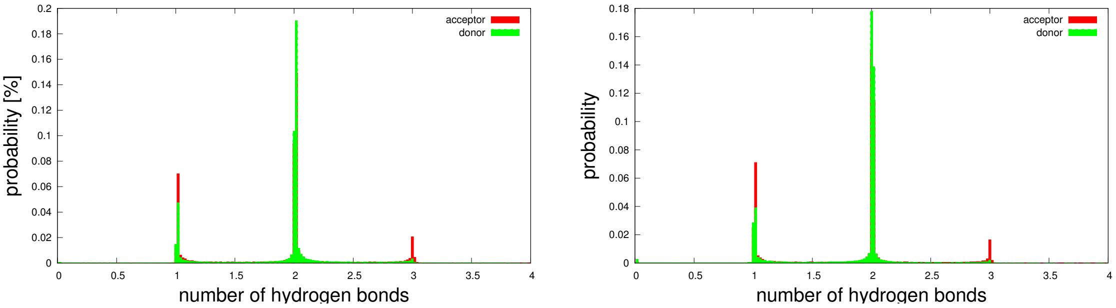

(g) System 3 - oxygen **(h)** System 4 - oxygen

Figure 3.10.: Analysis of hydrogen bonding in the water bulk.

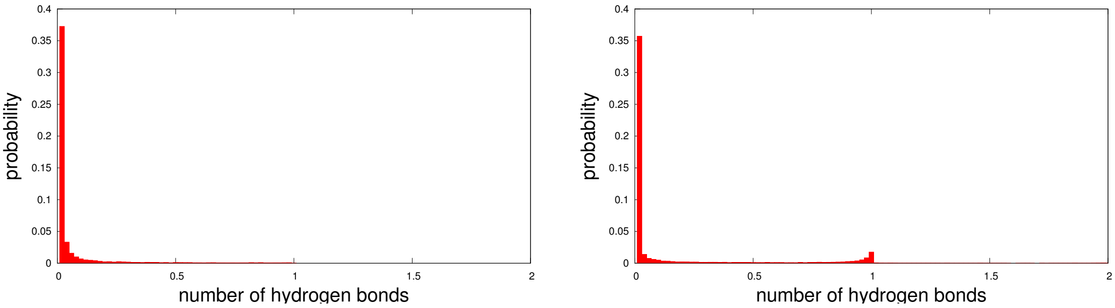

(a) System 2 - nitrogen

(b) System 3 - nitrogen

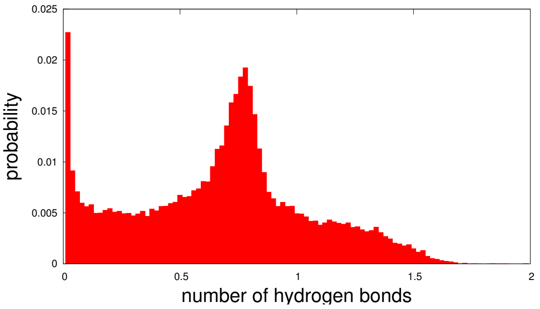

(c) System 4 - nitrogen

Figure 3.11.: Historgrams of the probability of nitrogen atoms forming hydrogen bonds.

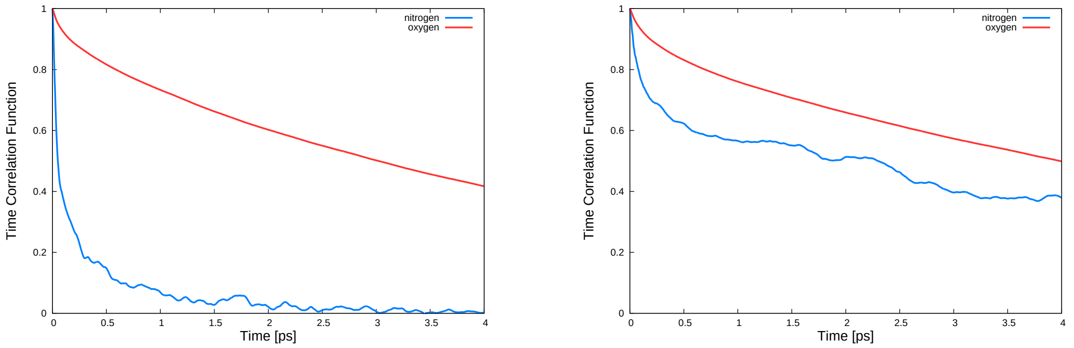

(a) System 3

(b) System 4

Figure 3.12.: The time autocorrelation function of the number of hydrogen bonds in Systems 3 and 4. The blue line is the autocorrelation function of the hydrogen bonds between water and nitrogen and the red line describes the autocorrelation function of the hydrogen bonds in the water bulk.

also emphasise the weakness of the hydrogen bonds with nitrogen as a hydrogen bond acceptor compared with the hydrogen bonds between water molecules. The decay of the hydrogen bonds between water and nitrogen is very fast compared in system 3 as compared to the decay in system 4. The number of hydrogen bonds between water and substitutional nitrogen atoms is not only much lower compared to the pyridine-type nitrogen atoms in system 4. The hydrogen bonds are also much weaker and easily broken.

3.5. Electronic Structure

To characterize these hydrogen bonds, one structure in system 4 was invesitgated using DFT. The electron density was computed in a single-point calculation using the parameters descirbed in section 2.3. The configuration chosen at 3.837 ps has one of the smalles N-H distances with 1.83 Å. Figure 3.13 shows the configuration with the respective electron density surfaces. The other panel (figure 3.13a) shows the electron density in a plane in the graphene sheet.

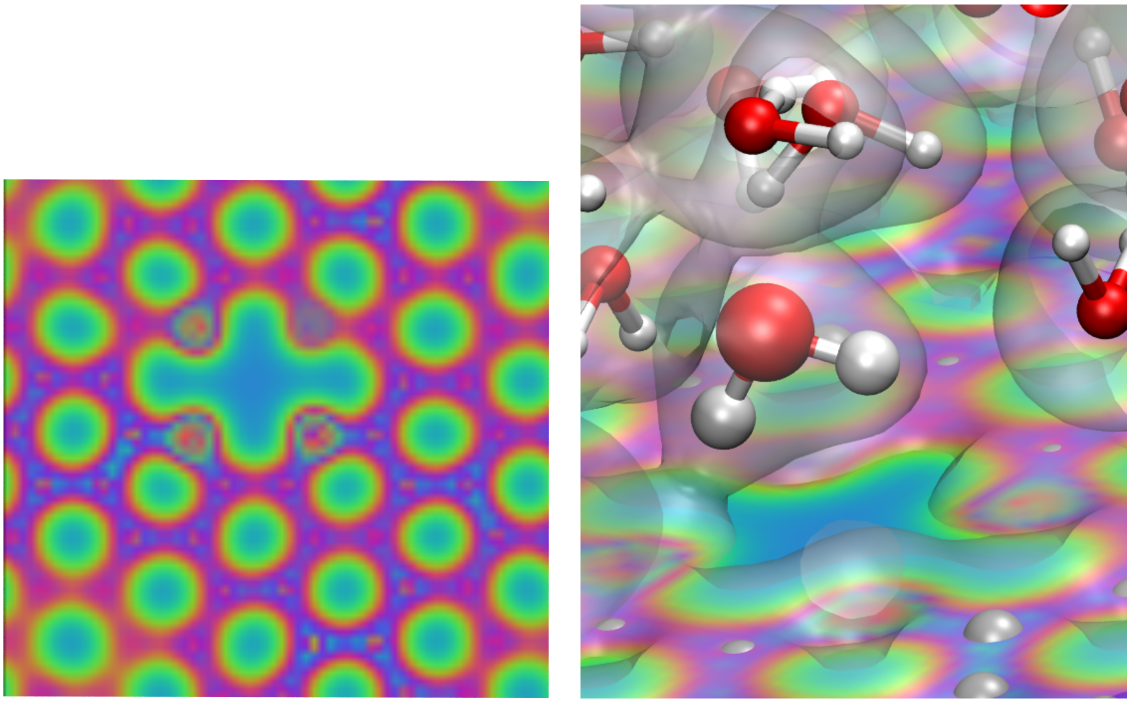
(a)

(b)

Figure 3.13.: (a) The electron density in one plane of the graphene sheet. (b) The isosurface of the electron density for one configuration of system 4

The electron density in the graphene shee depicted in figure 3.13a shows the disruption of the pristine graphene surface quite well. The divacancy causes a large hole in the honeycomb structure of the graphene surface and its otherwise highly regular electron density. An the pyridinic nitrogen atoms at the corners have a larger electron density than the surrounding carbon atoms.

The electronic structure calulations show the overlap in the electron density for the large water molecule with the pyridinic nitrogen atom. This shows the weak and highly dynamic hydrogen bonding between the water molecules and the nitrogen doped surface. Remarkable about this bonded water molecule is the fact, that it not only has one dangling O-D bond pointing towards and bonding with the surface. Its second O-D bond points at the surface as well. Water molecules pointing two of their O-D bonds towards the surface could not be observed for any of the other systems.

The electronic structure calculations underline the reactivity of the pyridine-type nitrogen defects. The hydrogen bonds indicated by the other analytical methods of the MD simulations are confirmed by the overlap of the electron densities and the bonding implied therein.

4. Conclusions

Hydrogen as an environmetally friendly energy carrier has gained much attention lately. Combustion of hydrogen only yields water as a product and no greenhouse gases, like the combustion of fossil fuels. Electrolysis of water yields oxygen and hydrogen by splitting it electrochemically. The efficiency of the electrolysis process is limited by the high overpotential of the OER (equation 4.1):

$$2H_2O \longrightarrow O_2 + 4H^+ + 4e^- \tag{4.1}$$

The overpotential for this reaction is about 450 mV using commercial nickel electrodes. This overpotential can be lowered by using electrodes containin rhodium or iridium oxide. These metals are very precius and rare and therefore very expensive. Novel graphene materials doped with nitrogen are also able to function as electrocatalysts for this reduction and lower the overpotential to 380 mV. The graphene materials are inexpensive and as efficient as the rhodium and iridium catalysts. The catalytic activity is attributed to the nitrogen-doping sites in the material and two types of nitrogen defects were characterized in the experiment: the substitutional and the pyridine-type defects.

Using two different substitutional patterns, the interaction of water with these graphene material was studied. Molecular dynamics simulations of water confined between four different graphene surfaces (figure 4.1) were carried out. One undoped surface, two substitutional nitrogen defects with two and four nitrogen atoms each, as well as a graphene surface with a tetramerized pyridine-type defect were studied.

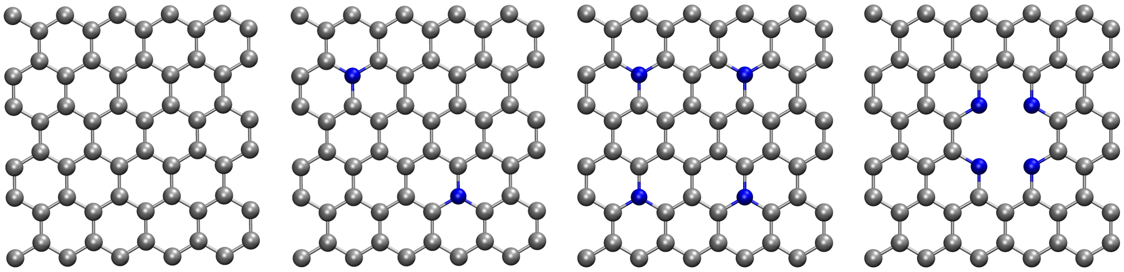

(a) System 1 **(b)** System 2 **(c)** System 3 **(d)** System 4

Figure 4.1.: Nitrogen substitution patterns of the studied graphene surfaces.

The molecular dynamics simulations were analyzed and the results show a clear tendency. The interaction of water with the undoped graphene sheet is very weak, as seen in previous calculations.[26] There is an exclusion volume of about 2 Å between the water and the graphene surface. Some water molecules in the surface layer merely show a tendency to point one O-D bond toward the surface and not engage that bond in hydrogen bonding with the other water molecules. This behavior was also seen for systems 2 and 3 with the substitutional nitrogen defects. Very weak and scarce hydrogen bonding between water molecules from the surface layer and the nitrogen atoms can be observed in system 3.

System 4 with four pyridine-type nitrogen defects located around a divacancy however shows a distinct interaction with water molecules from the interfacial layer. The water molecules enter the exclusion volume above the pyridine-type defect and engage in distinct hydrogen bonding with the nitrogen atoms. These hydrogen bonds are not as strong as the ones in the water bulk but still prevalent and pronounced. This distinct interaction of the confined water molecules with the pyridine-type nitrogen atoms in the graphene surface suggests, that these pyridine-type nitrogen atoms are responsible for the catalytic activity. And increasing the number of pyridine-type defects in the graphene materials would improve their catalytic activity even further.

A. Abbreviations

AIMD	*Ab initio* Molecular Dynamics
BOMD	Born-Oppenheimer molecular dynamics
CP2K	program package for *ab initio* molecular dynamics
DFT	density functional theory
diPy	dimerized pyridine-type defect
EASA	electrochemical active surface area
Eq.	equation
et al.	et alii (latin, and others)
FFT	fast-Fourier transform
Fig.	figure
GGA	generalized gradient approximation
GPW	Gaussian and Plane wave method
GSA	geometric surface area
GTH	pseudopotential developed by Godecker, Teter Hutter
LDA	local density approximation
MD	molecular dynamics
monoPy	monomeric pyridine-type defect
NHE	normal hydrogen electrode
OER	oxygen evolution reaction
ORR	oxygen reduction reaction
PBE	Perdew, Burke and Ernzerhof
RDF	radial distribution function
subst	substitutional nitrogen defect
Tab.	table
tetraPy	tetramerized pyridine-type defect
triPy	trimerized pyridine-type defect
TZV2P	triple ζ valence basis set with double polarization
XPS	X-ray photoelectron spectroscopy

B. Data

The data CD contains the electronic version of this thesis, the trajectories of the MD simulations for each system and the electron density file for the DFT calculation. All the trajectories as well as the cube denisty file can be visualized with VMD.

Bibliography

[1] Erwin Riedel and Christoph Janiak. *Anorganische Chemie.* de Gruyter, 7th edition edition, 2007.

[2] Dr. Ulrich Schmidtchen Prof. Jochen Lehmann, editor. *WASSERSTOFF DER NEUE ENERGIETRÄGER Eine fachliche Einführung vom Deutschen Wasserstoff- und Brennstoffzellen-Verband e.V. DWV.* Hydrogeit Verlag, Oberkrämer, 2015.

[3] Alex Izgorodin, Ekaterina Izgorodina, and Douglas R. MacFarlane. Low overpotential water oxidation to hydrogen peroxide on a mnox catalyst. *Energy Environ. Sci.*, 5:9496–9501, 2012.

[4] Peter W. Atkins and Julio de Paula. *Physikalische Chemie.* Wiley-VCH, Weinheim, 5. auflage märz 2013 edition, 2013.

[5] Michael G. Walter, Emily L. Warren, James R. McKone, Shannon W. Boettcher, Qixi Mi, Elizabeth A. Santori, and Nathan S. Lewis. Solar water splitting cells. *Chemical Reviews*, 110(11):6446–6473, 2010. PMID: 21062097.

[6] Henri Bernard Beer. The invention and industrial development of metal anodes. *Journal of the Electrochemical Society*, 127:303C – 307C, 1980.

[7] S Trasatti. Electrocatalysis: understanding the success of dsa. *Electrochimica Acta*, 45:2377 – 2385, 2000.

[8] Feng Jiao and Heinz Frei. Nanostructured cobalt and manganese oxide clusters as efficient water oxidation catalysts. *Energy Environ. Sci.*, 3:1018–1027, 2010.

[9] Mohammad Mahdi Najafpour, Till Ehrenberg, Mathias Wiechen, and Philipp Kurz. Calcium manganese(iii) oxides ($camn_2o_4 \cdot x\ h_2o$) as biomimetic oxygen-evolving catalysts. *Angewandte Chemie International Edition*, 49(12):2233–2237, 2010.

[10] David M. Robinson, Yong Bok Go, Martha Greenblatt, and G. Charles Dismukes. Water oxidation by mno_2: Catalysis by the cubical mn_4o_4 subcluster obtained by delithiation of spinel $limn_2o_4$. *Journal of the American Chemical Society*, 132(33):11467–11469, 2010. PMID: 20672802.

[11] G.L. Elizarova, G.M. Zhidomirov, and V.N. Parmon. Hydroxides of transition metals as artificial catalysts for oxidation of water to dioxygen. *Catalysis Today*, 58:71 – 88, 2000.

[12] Matthew W. Kanan and Daniel G. Nocera. In situ formation of an oxygen-evolving catalyst in neutral water containing phosphate and co^{2+}. *Science*, 321(5892):1072–1075, 2008.

[13] James B. Gerken, J. Gregory McAlpin, Jamie Y. C. Chen, Matthew L. Rigsby, William H. Casey, R. David Britt, and Shannon S. Stahl. Electrochemical water oxidation with cobalt-based electrocatalysts from ph 14: The thermodynamic basis for catalyst structure, stability, and activity. *Journal of the American Chemical Society*, 133(36):14431–14442, 2011. PMID: 21806043.

[14] J. Gregory McAlpin, Yogesh Surendranath, Mircea Dincă, Troy A. Stich, Sebastian A. Stoian, William H. Casey, Daniel G. Nocera, and R. David Britt. Epr evidence for co(iv) species produced during water oxidation at neutral ph. *Journal of the American Chemical Society*, 132(20):6882–6883, 2010.

[15] Yong Zhao, Ryuhei Nakamura, Kazuhide Kamiya, Shuji Nakanishi, and Kazuhito Hashimoto. Nitrogen-doped carbon nanomaterials as non-metal electrocatalysts for water oxidation. *Nature Communications*, 4:3390, August 2013.

[16] US Department of Energy and U.S. DRIVE Partnership. Hydrogen production technical team roadmap, June 2013.

[17] EUROPEAN COMMISSION. Hyways – the european hydrogen roadmap, 2008.

[18] Takashi Ikeda, Mauro Boero, Sheng-Feng Huang, Kiyoyuki Terakura, Masaharu Oshima, and Jun-ichi Ozaki. Carbon alloy catalysts: Active sites for oxygen reduction reaction. *The Journal of Physical Chemistry C*, 112(38):14706–14709, 2008.

[19] Heejin Kim, Kirak Lee, Seong Ihl Woo, and Yousung Jung. On the mechanism of enhanced oxygen reduction reaction in nitrogen-doped graphene nanoribbons. *Phys. Chem. Chem. Phys.*, 13:17505–17510, 2011.

[20] Khaled Parvez, Shubin Yang, Yenny Hernandez, Andreas Winter, Andrey Turchanin, Xinliang Feng, and Klaus Müllen. Nitrogen-doped graphene and its iron-based composite as efficient electrocatalysts for oxygen reduction reaction. *ACS Nano*, 6(11):9541–9550, 2012. PMID: 23050839.

[21] Lipeng Zhang and Zhenhai Xia. Mechanisms of oxygen reduction reaction on nitrogen-doped graphene for fuel cells. *The Journal of Physical Chemistry C*, 115(22):11170–11176, 2011.

[22] Michikazu Hara, Chad C. Waraksa, John T. Lean, Bradley A. Lewis, and Thomas E. Mallouk. Photocatalytic water oxidation in a buffered tris(2,2'-bipyridyl)ruthenium complex-colloidal iro$_2$ system. *The Journal of Physical Chemistry A*, 104(22):5275–5280, 2000.

[23] Yoshitaka Fujimoto and Susumu Saito. Formation, stabilities, and electronic properties of nitrogen defects in graphene. *Phys. Rev. B*, 84:245446, Dec 2011.

[24] M. K. Kostov, E. E. Santiso, A. M. George, K. E. Gubbins, and M. Buongiorno Nardelli. Dissociation of water on defective carbon substrates. *Phys. Rev. Lett.*, 95:136105, Sep 2005.

[25] Manu Sharma, Davide Donadio, Eric Schwegler, and Giulia Galli. Probing properties of water under confinement: Infrared spectra. *Nano Letters*, 8(9):2959–2962, 2008. PMID: 18680386.

[26] Giancarlo Cicero, Jeffrey C. Grossman, Eric Schwegler, Francois Gygi, and Giulia Galli. Water confined in nanotubes and between graphene sheets: A first principle study. *Journal of the American Chemical Society*, 130(6):1871–1878, 2008. PMID: 18211065.

[27] R. R. Q. Freitas, R. Rivelino, F. de Brito Mota, and C. M. C. de Castilho. Dft studies of the interactions of a graphene layer with small water aggregates. *The Journal of Physical Chemistry A*, 115(44):12348–12356, 2011. PMID: 21954939.

[28] L. Cheng, P. Fenter, K. L. Nagy, M. L. Schlegel, and N. C. Sturchio. Molecular-scale density oscillations in water adjacent to a mica surface. *Phys. Rev. Lett.*, 87:156103, Sep 2001.

[29] Song Hi Lee and Peter J. Rossky. A comparison of the structure and dynamics of liquid water at hydrophobic and hydrophilic surfaces – a molecular dynamics simulation study. *The Journal of Chemical Physics*, 100(4):3334–3345, 1994.

[30] Chyuan-Yih Lee, J. Andrew McCammon, and P. J. Rossky. The structure of liquid water at an extended hydrophobic surface. *The Journal of Chemical Physics*, 80(9):4448–4455, 1984.

[31] P. Hohenberg and W. Kohn. Inhomogeneous electron gas. *Phys. Rev.*, 136:B864–B871, Nov 1964.

[32] W. Kohn and L. J. Sham. Self-consistent equations including exchange and correlation effects. *Phys. Rev.*, 140:A1133–A1138, Nov 1965.

[33] R. P. Feynman. Forces in molecules. *Phys. Rev.*, 56:340–343, Aug 1939.

[34] Loup Verlet. Computer "experiments" on classical fluids. i. thermodynamical properties of lennard-jones molecules. *Phys. Rev.*, 159:98–103, Jul 1967.

[35] J. Kolafa. Time-reversible always stable predictor-corrector method for molecular dynamics of polarizable molecules. *Journal of Computational Chemistry*, 25(3):335–342, 2004.

[36] Hans C. Andersen. Molecular dynamics simulations at constant pressure and/or temperature. *The Journal of Chemical Physics*, 72(4):2384–2393, 1980.

[37] Shuichi Nose. A unified formulation of the constant temperature molecular dynamics methods. *The Journal of Chemical Physics*, 81(1):511–519, 1984.

[38] Shuichi Nose. A molecular dynamics method for simulations in the canonical ensemble. *Molecular Physics*, 52(2):255–268, 1984.

[39] Giovanni Bussi, Davide Donadio, and Michele Parrinello. Canonical sampling through velocity rescaling. *The Journal of Chemical Physics*, 126(1):–, 2007.

[40] Juerg Hutter, Matthias Krack, Teodoro Laino, Joost VandeVondele, Andreas Gloess, Alfio Lazzaro, Michele Ceriotti, Christopher J. Mundy, Mauro Del Ben, Dorothea Golze, Florian Schiffmann, M. H. Bani-Hashemian, Harald Forbert, Iain Bethune, Lukasz Walewski, Marcella Iannuzzi, Matt McGrath, Ole Schütt, Christiane Pousa Ribeiro, Vladimir Rybkin, Samuel Andermatt, Thomas D. Kühne, Urban Borstnik, and William Kuo. Cp2k open source molecular dynamics. `http://www.cp2k.org/`, 2013.

[41] Joost VandeVondele, Matthias Krack, Fawzi Mohamed, Michele Parrinello, Thomas Chassaing, and Jörg Hutter. Quickstep: Fast and accurate density functional calculations using a mixed gaussian and plane waves approach. *Computer Physics Communications*, 167(2):103 – 128, 2005.

[42] John P. Perdew, Kieron Burke, and Matthias Ernzerhof. Generalized gradient approximation made simple. *Phys. Rev. Lett.*, 77:3865–3868, Oct 1996.

[43] Gerald Lippert, Jurg Hutter, and Michele Parrinello. A hybrid gaussian and plane wave density functional scheme. *Molecular Physics*, 92(3):477–488, 1997.

[44] M. Krack. Pseudopotentials for h to kr optimized for gradient-corrected exchange-correlation functionals. *Theoretical Chemistry Accounts*, 114(1-3):145–152, 2005.

[45] C. Hartwigsen, S. Goedecker, and J. Hutter. Relativistic separable dual-space gaussian pseudopotentials from h to rn. *Phys. Rev. B*, 58:3641–3662, Aug 1998.

[46] S. Goedecker, M. Teter, and J. Hutter. Separable dual-space gaussian pseudopotentials. *Phys. Rev. B*, 54:1703–1710, Jul 1996.

[47] M. Frigo and S.G. Johnson. The design and implementation of fftw3. *Proceedings of the IEEE*, 93(2):216–231, Feb 2005.

[48] Joost VandeVondele and Jörg Hutter. Gaussian basis sets for accurate calculations on molecular systems in gas and condensed phases. *The Journal of Chemical Physics*, 127(11):–, 2007.

[49] Joost VandeVondele and Jörg Hutter. An efficient orbital transformation method for electronic structure calculations. *The Journal of Chemical Physics*, 118(10):4365–4369, 2003.

[50] Jeffrey C. Grossman, Eric Schwegler, Erik W. Draeger, FranÃ§ois Gygi, and Giulia Galli. Towards an assessment of the accuracy of density functional theory for first principles simulations of water. *The Journal of Chemical Physics*, 120(1):300–311, 2004.

[51] Eric Schwegler, Jeffrey C. Grossman, FranÃ§ois Gygi, and Giulia Galli. Towards an assessment of the accuracy of density functional theory for first principles simulations of water. ii. *The Journal of Chemical Physics*, 121(11):5400–5409, 2004.

[52] Toni Giorgino. Computing 1-d atomic densities in macromolecular simulations: The density profile tool for {VMD}. *Computer Physics Communications*, 185(1):317 – 322, 2014.

[53] Piero Gasparotto and Michele Ceriotti. Recognizing molecular patterns by machine learning: An agnostic structural definition of the hydrogen bond. *The Journal of Chemical Physics*, 141(17):174110, 2014.

Erklärung

Hiermit versichere ich, dass ich diese Arbeit selbständig verfasst und keine anderen, als die angegebenen Quellen und Hilfsmittel benutzt, die wörtlich oder inhaltlich übernommenen Stellen als solche kenntlich gemacht habe.

Mainz, den 03.07.2015